THE JOURNAL OF PHYSICAL CHEMISTRY A

Article

Cite This: J. Phys. Chem. A 2019, 123, 3655−3671

pubs.acs.org/JPCA

Temperature Dependence Study of the Kinetics and Product Yields of the $HO_2 + CH_3C(O)O_2$ Reaction by Direct Detection of OH and HO_2 Radicals Using 2f-IR Wavelength Modulation Spectroscopy

Published as part of The Journal of Physical Chemistry virtual special issue "Hanna Reisler Festschrift".

Aileen O. Hui,*,† Mathieu Fradet,*,‡ Mitchio Okumura,*,† and Stanley P. Sander*,‡

†Arthur Amos Noyes Laboratory of Chemical Physics, Division of Chemistry and Chemical Physics, California Institute of Technology, M/S 127-72, 1200 East California Boulevard, Pasadena, California 91125, United States

‡Jet Propulsion Laboratory, California Institute of Technology, 4800 Oak Grove Drive, Pasadena, California 91109, United States

Supporting Information

ABSTRACT: The $HO_2 + CH_3C(O)O_2$ reaction consists of three product channels: $CH_3C(O)OOH + O_2$ (R1a), $CH_3C(O)OH + O_3$ (R1b), and $OH + CH_3C(O)O + O_2$ (R1c). The overall rate constant (k_1) and product yields (α_{1a}, α_{1b}, and α_{1c}) were determined over the atmospherically relevant temperature range of 230−294 K at 100 Torr in N_2. Time-resolved kinetics measurements were performed in a pulsed laser photolysis experiment in a slow flow cell by employing simultaneous infrared (IR) and ultraviolet (UV) absorption spectroscopy. HO_2 and $CH_3C(O)O_2$ were formed by Cl-atom reactions with CH_3OH and CH_3CHO, respectively. Heterodyne near- and mid-infrared (NIR and MIR) wavelength modulation spectroscopy (WMS) was employed to selectively detect HO_2 and OH radicals. Ultraviolet absorption at 225 and 250 nm was used to detect various peroxy radicals as well as ozone (O_3). These experimental techniques enabled direct measurements of α_{1c} and α_{1b} via time-resolved spectroscopic detection in the MIR and the UV, respectively. At each temperature, experiments were performed at various ratios of initial HO_2 and $CH_3C(O)O_2$ concentrations to quantify the secondary chemistry. The Arrhenius expression was found to be $k_1(T) = 1.38^{+1.17}_{-0.63} \times 10^{-12} \exp[(730 \pm 170)/T]$ cm^3 molecule^{-1} s^{-1}. α_{1a} was temperature-independent while α_{1b} and α_{1c} decreased and increased, respectively, with increasing temperatures. These trends are consistent with the current recommendation by the IUPAC data evaluation. Hydrogen-bonded adducts of HO_2 with the precursors, $HO_2{\cdot}CH_3OH$ and $HO_2{\cdot}CH_3CHO$, played a role at lower temperatures; as part of this work, rate enhancements of the HO_2 self-reaction due to reactions of the adducts with HO_2 were also measured.

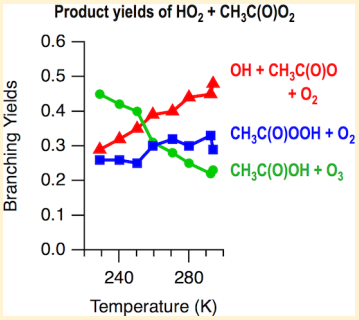

1. INTRODUCTION

Organic peroxy radicals (RO_2), important intermediates in the Earth's atmosphere, are formed from the oxidation of volatile organic compounds (VOCs). RO_2 plays a key role in the tropospheric HO_x ($HO_x \equiv HO_2 + OH$) cycle, and its chemistry influences the formation of tropospheric O_3 and other secondary pollutants. In polluted regions (i.e., high $NO_x \equiv NO + NO_2$), the predominant sink for RO_2 is reaction with NO, which primarily propagates radical chemistry by recycling NO_2 and OH radicals. During the day, NO_2 photolysis produces O_3, which is the primary constituent of photochemical smog. In remote regions of the atmosphere where NO_x concentrations are low, reactions of RO_2 with HO_2, OH, and other RO_2 radicals become increasingly important loss processes for RO_2.

Reactions of RO_2 with HO_2 are of particular interest because the product distribution depends on the structure of the R group. Although $HO_2 + RO_2$ reactions were initially thought to be radical terminating processes, more recent studies have shown that for some more complex peroxy radicals, the reaction can also produce OH radicals via a radical propagating channel, effectively sustaining the oxidative capacity of the atmosphere.

$$HO_2 + RO_2 \rightarrow ROOH + O_2$$
$$\rightarrow ROH + O_3$$
$$\rightarrow OH + RO + O_2$$

$HO_2 + RO_2$ reactions that have an OH recycling channel are of atmospheric importance because they contribute to higher OH concentrations in VOC-rich regions. There is currently disagreement between modeled and observed OH levels over remote, forested regions of the Earth. Results from various field campaigns have demonstrated that in these regions, the level of the discrepancy appears to be positively correlated with concentrations of isoprene, which is an abundant chemically active biogenic compound.[2−6] While this discrepancy could be

Received: January 15, 2019
Revised: March 14, 2019
Published: April 3, 2019

DOI: 10.1021/acs.jpca.9b00442
J. Phys. Chem. A 2019, 123, 3655−3671

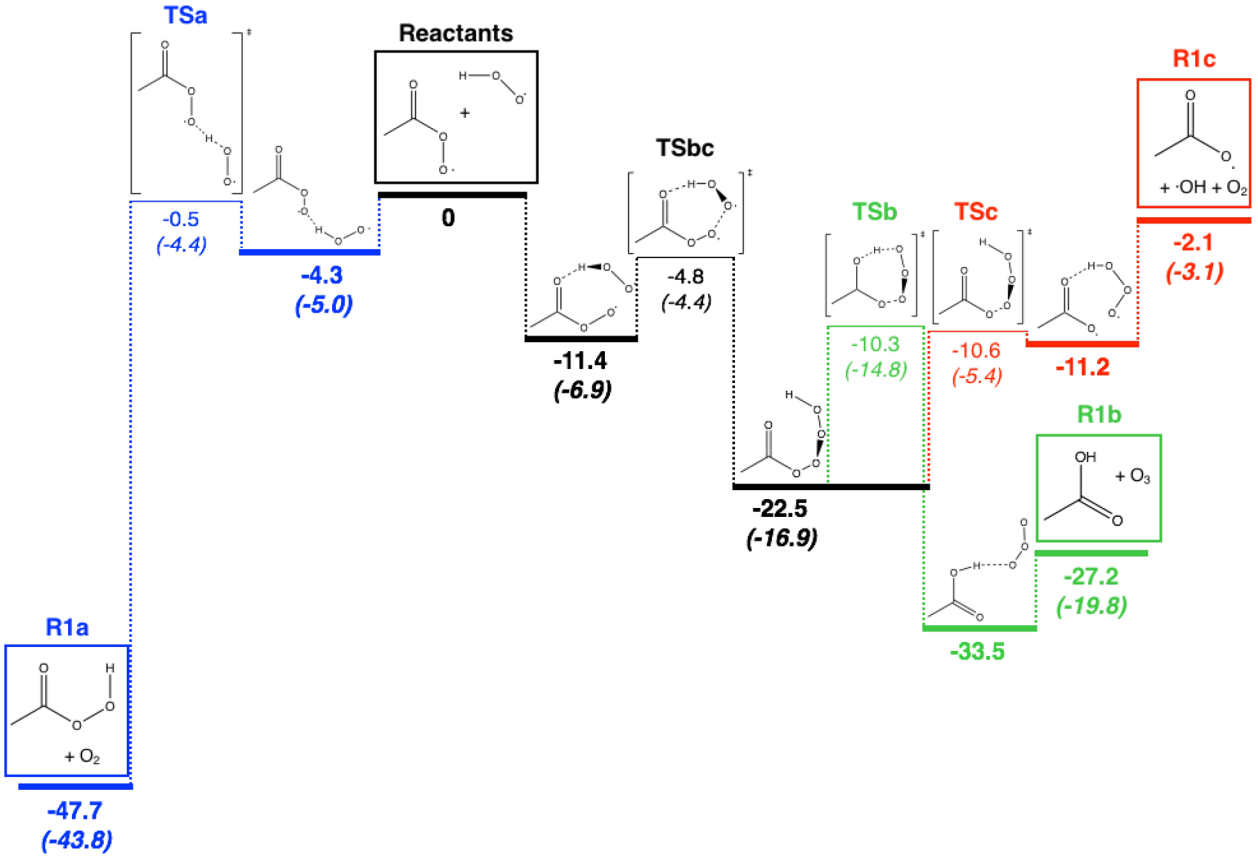

Figure 1. Simplified energy level diagram (energies in kcal mol^{-1}) of the HO_2 + $CH_3C(O)O_2$ reaction, modified from Hasson et al.[13] Only the most relevant structures are shown. Energies in parentheses, if provided, were taken from Le Crâne et al.[14] All other energies were taken from Hasson et al.[13] The triplet surface is shown in blue. The two product channels on the singlet surface are shown in red (R1c) and green (R1b). The part of the singlet surface that is common to (R1c) and (R1b) is shown in black.

Table 1. Summary of Previous HO_2 + $CH_3C(O)O_2$ Studies and Their Sensitivities to Key Chemical Species (R = $CH_3C(O)$)[a]

ref	method	T (K)	P (Torr)	HO_2	RO_2	OH	ROOH	O_3	ROH
Niki et al.[10,b]	FTIR	298	700				direct	direct	direct
Moortgat et al.[19,c]	FP/UVAS	253−368	600−650	UV	UV			UV	
Horie and Moortgat[11,d]	FTIR	263−333	730−770			direct	direct	direct	
Crawford et al.[20,c]	PLP/IR/UVAS	269−363	50	direct	UV			UV	
Tomas et al.[21,c]	FP/UVAS	273−403	760	UV	UV			UV	
Hasson et al.[9,c]	UVP/FTIR/HPLC	298	800				direct		direct
Le Crâne et al.[14,c]	FP/UVAS	298	760	UV	UV			UV	
Jenkin et al.[15,c]	UVP/FTIR	296	700			indirect	direct		direct
Dillon and Crowley[16,c]	PLP/LIF	298	75−529			direct			
Groß et al.[17,c]	PLP/LIF/UVAS	298	100−500	UV	UV	direct		UV	
Winiberg et al.[18,c]	UVP/FTIR/LIF	293	750	indirect		direct	direct	direct	direct
this work[c]	PLP/IR/UVAS	230−294	100	direct	UV	direct		UV	

[a]FP = flash photolysis; PLP = pulsed laser photolysis; UVAS = UV absorption spectroscopy; HPLC = high performance liquid chromatography; FTIR = Fourier transform infrared spectroscopy; LIF = laser induced fluorescence. [b]Reagent gases: $Cl_2/CH_2O/CH_3CHO/O_2/N_2$. [c]Reagent gases: $Cl_2/CH_3OH/CH_3CHO/O_2/N_2$. [d]Reagent gases: $CH_3C(O)C(O)CH_3/O_2$/Ar.

due to possible missing sources of OH in current atmospheric models, instrument-dependent artifacts in the OH measurements,[7,8] or a combination of both, a full picture of the radical chemistry in VOC-rich atmospheres requires further laboratory experiments.

One significant oxidation product of isoprene is the acetylperoxy radical, $CH_3C(O)O_2$. Hasson et al.[9] found that the reaction of $CH_3C(O)O_2$ with HO_2 includes an OH product channel:

$$HO_2 + CH_3C(O)O_2 \rightarrow CH_3C(O)OOH + O_2 \quad (R1a)$$

$$\rightarrow CH_3C(O)OH + O_3 \quad (R1b)$$

$$\rightarrow OH + CH_3C(O)O + O_2 \quad (R1c)$$

$CH_3C(O)O_2$ radicals play an important role in tropospheric chemistry because they are also formed from the photooxidation of a large variety of higher carbonyl compounds such as acetaldehyde, acetone, and other VOCs that are abundant in the atmosphere. Although this reaction may not fully resolve the

DOI: 10.1021/acs.jpca.9b00442
J. Phys. Chem. A 2019, 123, 3655−3671

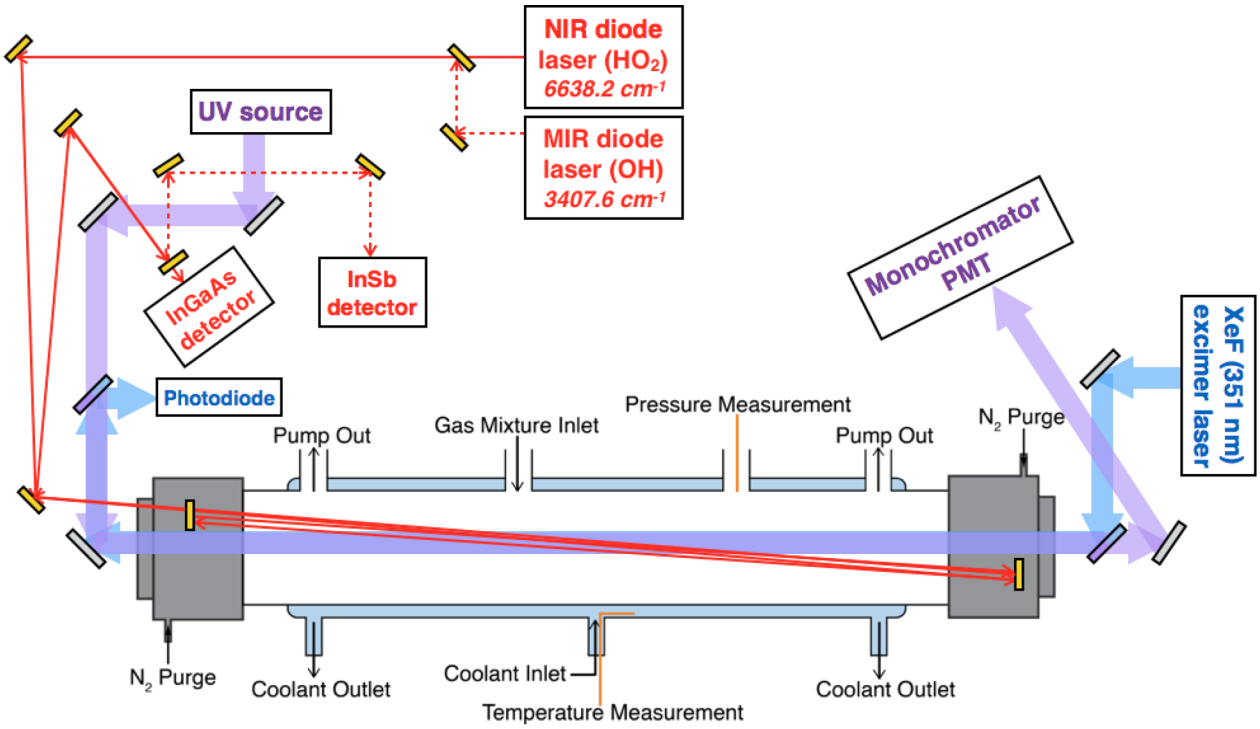

Figure 2. Schematic of the IRKS apparatus. A precooled gas mixture entered the temperature-controlled Pyrex flow tube, where radicals were generated by pulsed excimer laser photolysis (beam path shown in blue). Three independent absorption probe beams were used to temporally monitor the reactant and product species: NIR and MIR light (solid and dashed red lines) from two diode lasers was coupled to multipass Herriott optics, and broadband UV light made a single-pass through the reaction cell (purple). Flip mirrors were used (red rectangles) to switch between the two IR lasers.

OH discrepancy between the models and observations, this reaction still serves as an important benchmark system to study OH regeneration from HO_2 + RO_2 reactions in low NO_x environments.

(R1) has been the subject of a number of experimental studies and was initially thought to be exclusively radical terminating, based on end-product studies of stable products.[10,11] Hasson et al.[9] first inferred the OH product channel. A large OH yield had also been inferred for a similar reaction between HO_2 and $C_2F_5C(O)O_2$.[12] Subsequently, two independent quantum chemistry calculations[13,14] suggested that (R1) proceeds via one of two mechanisms: (1) hydrogen transfer on a triplet surface to form $CH_3C(O)OOH + O_2$ (R1a) or (2) formation of a hydrotetroxide (ROOOOH) intermediate followed by decomposition on a singlet surface to form either $CH_3C(O)OH + O_3$ (R1b) or $OH + CH_3C(O)O + O_2$ (R1c). The potential energy surfaces from both studies showed that R1c was less exothermic than (R1b). A simplified energy level diagram of (R1) modified from Hasson et al.[13] is shown in Figure 1. Note that only the most relevant structures are shown. The full energy level diagram with detailed structures can be found in Hasson et al.[13] The figure demonstrates the differences in the energies calculated by Hasson et al.[13] and Le Crâne et al.[14] Le Crâne et al.[14] cited the low exothermicity of (R1c) relative to (R1b) to explain the <0.1 yield of OH that was reported experimentally. However, Hasson et al.[13] performed master equation calculations which found that (R1c) is a significant product channel proceeding via a chemically activated $HO_2{\cdot}CH_3C(O)O_2$ adduct.

Since these revelations, both indirect[14,15] and direct[16−18] measurements of OH radicals from (R1c) have been made. Table 1 summarizes the experimental techniques employed by previous laboratory studies of (R1). Although a majority of these experimental studies reports a significant OH yield from (R1) and support Hasson et al.'s postulate,[13] there are discrepancies in the reported values. Chamber-type studies of this reaction produced valuable data in identifying and quantifying the stable species;[9−11,15,18] however, extracting accurate kinetics information from these studies is limited by the uncertainties in the rate coefficients of the secondary chemistry. Furthermore, with the exception of Winiberg et al.,[18] these studies also lacked direct sensitivity to reactive radical species. Meanwhile, many of the pulsed photolysis experiments of the title reaction have used UV absorption techniques, which can detect peroxy radicals with good sensitivity due to the large absorption cross sections. However, there is significant spectral overlap among the peroxy radicals, as well as with product species generated from unavoidable secondary chemistry. The spectral overlap necessitates deconvolution of the observed UV spectrum, which introduces additional systematic errors. Previous studies of this reaction utilizing laser-induced fluorescence (LIF) provided an extremely sensitive way of detecting OH radicals directly; however, no studies have yet used techniques that directly and selectively measure both OH and HO_2.

In addition, there are no temperature dependence studies of (R1c), which are needed in modeling studies of the upper troposphere. For example, the only experimental temperature dependence studies of both the kinetics and branching yields of (R1) assumed that the reaction was exclusively radical terminating,[19−21] which may have led to an underestimation of the reported overall rate constant, k_1. It is also important to note that temperature dependence studies using CH_3OH and CH_3CHO as precursors for HO_2 and $CH_3C(O)O_2$, respectively, may not have fully accounted for the formation of hydrogen-bonded adducts involving HO_2 and the radical precursors. The radical adducts, $HO_2{\cdot}CH_3OH$ and $HO_2{\cdot}CH_3CHO$, react at enhanced rates with HO_2, leading to a faster observed HO_2

DOI: 10.1021/acs.jpca.9b00442
J. Phys. Chem. A 2019, 123, 3655−3671

decay rate. Rate enhancement of the HO_2 self-reaction by these adducts contributes to the total loss rate of HO_2 and becomes more significant at low temperatures, where adduct formation is more favored.[22−24] The reactions of the adducts must be considered in order to measure k_1 correctly.

In the present work, we used infrared kinetic spectroscopy (IRKS) for sensitive and selective detection of several radical species. IRKS combines detection in the IR and UV to simultaneously monitor multiple species in real time. We determined the overall rate constant, k_1, and the product yields, α_{1a}, α_{1b}, and α_{1c}, where

$$\alpha_{1a} = k_{1a}/k_1 \qquad \alpha_{1b} = k_{1b}/k_1 \qquad \alpha_{1c} = k_{1c}/k_1 \tag{1}$$

and

$$k_1 = k_{1a} + k_{1b} + k_{1c} \tag{2}$$

In the near-IR (NIR) and mid-IR (MIR), we used a high resolution heterodyne technique, wavelength modulation spectroscopy (WMS), to selectively detect HO_2 and OH radicals, respectively. We generated HO_2 and $CH_3C(O)O_2$ radicals by pulsed laser photolysis (PLP) and measured the decay of HO_2 in the NIR and the formation and subsequent decay of OH in the MIR. Direct detection of HO_2 in the NIR and OH in the MIR allowed for accurate determination of k_1 and direct measurements of α_{1c}. Although traditional LIF techniques offer superior sensitivity to OH radicals, an advantage of IRKS is that the OH and HO_2 probes follow identical optical paths, removing biases that would otherwise be introduced from differences in diffusion, path lengths, etc., that result from probing different regions of the photolysis volume. In addition to NIR and MIR WMS, we also employed direct absorption spectroscopy in the UV to monitor the time dependence of various reactant and product species. Specifically, two wavelengths (λ = 225 nm and λ = 250 nm) were chosen to detect the peroxy radicals and O_3. Measurement of O_3 enabled direct determination of α_{1b}. Finally, α_{1a} was not measured directly, but was determined from the measured values of k_1, α_{1b}, and α_{1c}.

This study measured k_1, α_{1a}, α_{1b}, and α_{1c} over the temperature range 230−294 K at 100 Torr. At each temperature, experiments were conducted over a wide range of experimental conditions that varied in total and relative initial radical concentrations of HO_2 and $CH_3C(O)O_2$. This work reports the first experimental temperature dependence measurements of α_{1c} and also extends to lower temperatures the range of temperatures over which k_1 had been previously measured. We also present kinetics measurements of the adducts of HO_2 formed from the reaction of HO_2 with the radical precursors, CH_3OH and CH_3CHO.

2. EXPERIMENTAL METHODS

2.1. Overview of IRKS. The IRKS apparatus consisted of a temperature-controlled pulsed laser photolysis flow cell coupled to simultaneous spectroscopic detection in the UV and in the NIR or MIR (Figure 2). This technique has been used for studying the kinetics of various peroxy radicals and has been described in detail previously.[25−27] For this work, an additional diode laser operating in the MIR was introduced to the apparatus to enable direct detection of OH radicals. Back-to-back experiments were carried out, alternating between two diode lasers operating in the NIR and in the MIR. Gas temperatures, pressures, and flows were carefully monitored to ensure that the experimental conditions were identical for the two IR measurements. Pulsed 351 nm light (~250 mJ/pulse) from a XeF excimer laser (Compex 301) was directed coaxially through the flow cell to initiate the chemistry by photolyzing Cl_2 molecules in gas mixtures of $Cl_2/N_2/O_2/CH_3OH/CH_3CHO$. The photolysis beam cross-section was 2 cm × 1 cm.

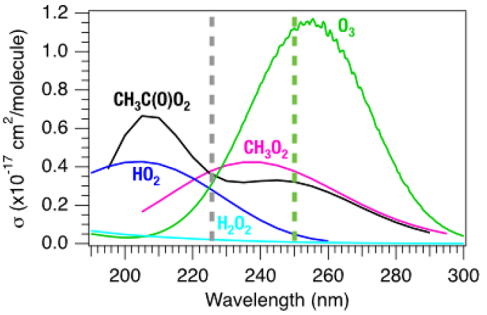

Figure 3. UV absorption cross sections of major reactant and product species generated in the present work.[28] Dashed lines indicate the wavelengths selected in this work.

Table 2. UV Absorption Cross Sections from JPL 15-10[29] (units: 10^{-20} cm^2)[a]

species	$\sigma_{\lambda=225nm}$	$\sigma_{\lambda=250nm}$
HO_2	288 ± 20	48.0 ± 4.6
H_2O_2	21.7 ± 1.1	8.3 ± 0.4
$CH_3C(O)O_2$	366 ± 23	322 ± 23
$CH_3C(O)$	1120	68
CH_3O_2	376 ± 27	378 ± 27
O_3	322 ± 6	1100 ± 22

[a]Uncertainties for HO_2, $CH_3C(O)O_2$, and CH_3O_2 were calculated from Tyndall et al.[30] All other uncertainties were taken from JPL 15-10.[29]

2.2. Flow Cell and Precursor Gases. Kinetics experiments were conducted in a jacketed Pyrex cell of length 175 cm and diameter 5 cm. The temperature inside the cell was controlled by flowing liquid nitrogen-cooled methanol circulating through the jacket of the cell and was measured with a type T thermocouple (Omega). Reagent gases were premixed and precooled in a Pyrex manifold prior to entering the cell. Room temperature N_2 purge gas flowed from the aluminum chambers on either end of the cell toward the gas pump-out ports to confine the main gas flow to the temperature-controlled region and to protect the Herriott mirrors that formed the multipass optical cavity for the IR probes. The gas flows were regulated by mass flow controllers (MKS Instruments), and the total flow rate was kept at approximately 2000 cm^3 (STP) min^{-1}, maintaining a 10 s residence time inside the flow cell at a total pressure of 100 ± 2 Torr. A photolysis repetition rate of 0.2 Hz was used, resulting in two photolysis events occurring per residence time. Decreasing the repetition rate to 0.1 Hz made no difference in the kinetics traces. CH_3OH and CH_3CHO were introduced into the cell by flowing N_2 through glass bubblers containing the liquid compounds, held inside temperature-controlled baths. The pressures in the reaction cell and bubblers were measured by absolute capacitance pressure gauges (MKS Baratron), and the concentrations of CH_3OH and CH_3CHO vapors were determined manometrically. Typical concentrations of the reagents were $[CH_3OH] = (2.0−8.8) \times 10^{15}$ molecules cm^{-3}, $[CH_3CHO] = (1.0−2.9) \times 10^{15}$ molecules cm^{-3}, $[O_2] = (1.6−2.0) \times 10^{18}$ molecules cm^{-3}, and $[Cl_2] = (2.3−3.8) \times 10^{15}$ molecules cm^{-3}. Total initial radical concentrations were typically $[Cl]_0 = (0.6−1.3) \times 10^{14}$ molecules cm^{-3}. More

DOI: 10.1021/acs.jpca.9b00442
J. Phys. Chem. A 2019, 123, 3655−3671

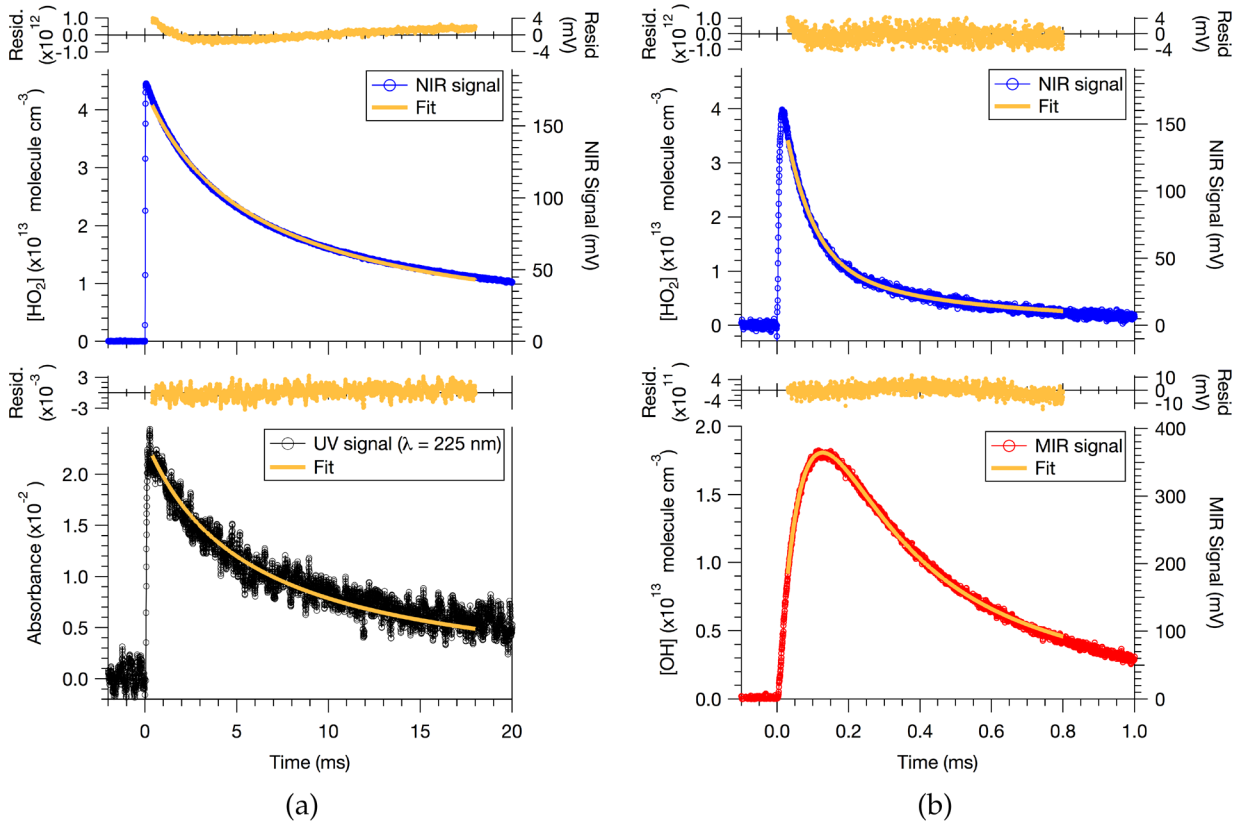

Figure 4. (a) Calibration of the 2f NIR (HO_2) signal. The NIR signal (top panel) and the UV absorbance signal at $\lambda = 225$ nm (bottom panel) from the $HO_2 + HO_2$ reaction were simultaneously fitted (orange trace) to determine V_{M,HO_2}. (b) Calibration of the 2f MIR (OH) signal. The MIR signal (top panel) and the calibrated NIR (HO_2) signal (bottom panel) from the HO_2 + NO reaction ([NO] = 1.2×10^{15} molecules cm^{-3}) were simultaneously fitted (orange trace) to determine $V_{M,OH}$. Residuals of the fits are shown above the data curves. Conditions: $T = 294$ K; $P = 100$ Torr; $[Cl]_0 = 4.4 \times 10^{13}$ molecules cm^{-3}; $[CH_3OH] = 4.5 \times 10^{15}$ molecules cm^{-3}.

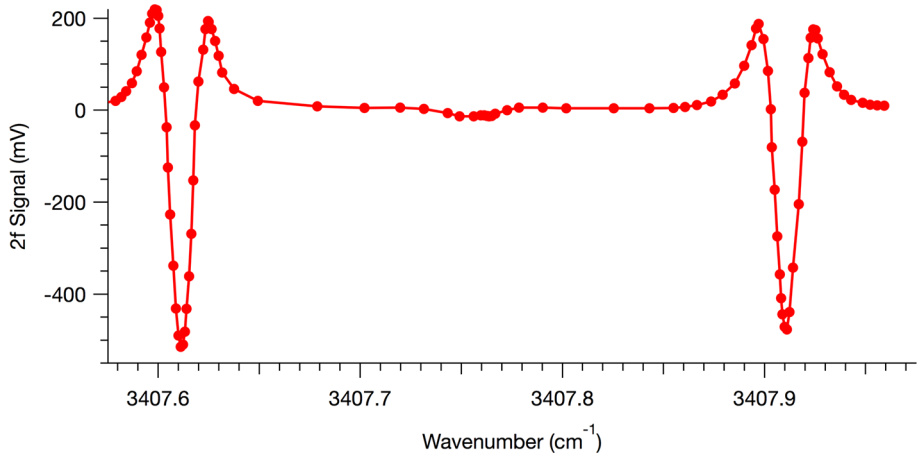

Figure 5. 2f signals of the MIR laser scanned across the OH doublets, obtained from the HO_2 + NO. The small dips between the OH lines are the weak absorption lines of HO_2.

details of the experimental conditions are provided in the Supporting Information.

2.3. UV Probe. Collimated broadband UV light from a laser-driven light source (Energetiq EQ-99XFC) was coaligned with and counter-propagated the excimer beam, making a single pass through the cell with an effective path length of 147 ± 10 cm. A monochromator (Acton Research Corporation Spectra Pro-300i) coupled to a photomultiplier tube (PMT) was used for wavelength-specific detection of the transmitted light. The slit width was typically set to 130 μm. The monochromator was calibrated against atomic emission lines from Hg, Cd, and Zn penray lamps. Baffles were placed on both ends of the flow cell to ensure that only light that sampled the photolysis volume entered the monochromator.

Using only the UV absorption signal to characterize (R1) introduces systematic errors due to spectral interference of various RO_2 and product species (Figure 3). However, simultaneous fits of the NIR, MIR, and UV signals placed

DOI: 10.1021/acs.jpca.9b00442
J. Phys. Chem. A 2019, 123, 3655−3671

additional constraints on the multiparameter fits. UV signals at 225 and 250 nm were collected back-to-back, each obtained simultaneously with either the NIR or MIR signal.

Sensitivity of the UV data to various peroxy radicals could be achieved by taking advantage of the differences in the UV absorption cross sections at these two wavelengths (Table 2). At 250 nm, absorption by O_3 dominates the total absorbance signal since the absorption cross-section of O_3 is at least a factor of ~3 times higher than those of other absorbing species. However, the 225 nm signal includes absorption by HO_2, CH_3O_2, and $CH_3C(O)O_2$. While the UV absorption cross sections of CH_3O_2 at 225 and 250 nm are nearly identical, the cross sections of $CH_3C(O)O_2$ are slightly different at the two wavelengths. Contribution of HO_2 to the total absorbance could be subtracted using the NIR data; therefore, simultaneous analysis of the NIR data with the two UV absorbance signals provided information about the relative concentration of $CH_3C(O)O_2$ to CH_3O_2. Although using wavelengths shorter than 225 nm would have facilitated the separation of $CH_3C(O)O_2$ from CH_3O_2 in the UV absorption measurements, the reduction in the UV lamp output below 220 nm would have caused significant decrease in the signal-to-noise.

2.4. IR Probes. Two continuous-wave (CW) distributed feedback (DFB) lasers operating in the NIR (3 mW) and MIR (10 mW), both manufactured by the Microdevices Laboratory (MDL) at the Jet Propulsion Laboratory (JPL), were used for selective detection of HO_2 and OH radicals, respectively. The NIR laser has been used in previous works and a detailed description can be found elsewhere.[25] The MIR laser was developed specifically for the experiments described in this work. In order to target the OH absorption line near 2.935 μm, a newly developed GaSb-based diode laser structure that was designed and grown at the National Research Council of Canada (NRC) was used. The targeted wavelength is reached slightly above room temperature, corresponding to over 10 mW of optical output power, and a side-mode suppression ratio greater than 25 dB. The architecture and details of the performance of this device is provided in Fradet et al.[31]

Experiments with the NIR and MIR probes were carried out back-to-back, using flip mirrors to switch between the two diode lasers and the corresponding detectors. Both the NIR and MIR beams were focused, collimated, and spatially filtered prior to entering the cell. Protected gold Herriott mirrors placed on either end of the cell folded the optical paths of the IR beams, enabling 30 passes inside the cell to amplify the path length to approximately 2700 cm. InGaAs (New Focus 1811) and InSb (Infrared Associates IS-0.25) photodiode detectors were used to detect the transmitted NIR and MIR light, respectively.

Both IR lasers were wavelength modulated at 6.8 MHz by using an external function generator to modulate the injection current. 2f-heterodyne detection was implemented by demodulating the detected signal at 13.6 MHz. The demodulated signal was amplified by a factor of 200. For a typical experimental run, the demodulated HO_2 and OH signals were collected at a sampling rate of 2.5 MHz at a bandwidth of 1 MHz, and averaged for 40 and 75 excimer laser shots, respectively. Since WMS only measures the relative changes in concentration, the NIR and MIR lasers were calibrated daily to obtain absolute concentrations of HO_2 and OH, respectively. The calibration procedure for each laser is described in detail below.

2.4.1. NIR Calibration. The NIR laser probed a blended group of rovibrational transitions in the first overtone of the O—H stretch of HO_2 ($2\nu_1$: 6638.2 cm^{-1}). The NIR signal was calibrated against the absolute concentration of HO_2 determined by its UV absorption cross-section at λ = 225 nm by measuring the NIR and UV decay signals simultaneously when HO_2 was the only peroxy radical present (Figure 4a). Despite a different geometric overlap due to the off-axis orientation of the Herriott mirrors, the IR and UV probe beams should capture the same physical processes at relatively short time scales (<20 ms); i.e., before diffusion becomes a significant loss process. At the beginning of every experiment, the kinetics traces from the HO_2 self-reaction were collected at three different initial radical concentrations at room temperature. The IR and UV traces were simultaneously fit to a bimolecular decay with the kinetics modeling program, FACSIMILE,[32] to obtain the calibration factor, V_{M,HO_2}, which relates the IR signal in mV (S_{HO_2}) to the absolute HO_2 concentration:

$$[HO_2] = S_{HO_2} \times V_{M,HO_2} \quad (3)$$

The fitted values of V_{M,HO_2} from the kinetics traces obtained from the three initial radical concentrations agreed within 5%. The systematic residuals in the NIR HO_2 signal in Figure 4a were attributed to the off-axis geometry of the NIR beam, which passes in and out of the photolysis volume, as well as the rise time of the detection electronics. On an absolute basis, the systematic residuals were small (2%) and did not affect the data analysis. The noise-equivalent concentration per $Hz^{-1/2}$ (NEC $Hz^{-1/2}$) of HO_2 normalized to one excimer shot was 2.9×10^9 molecules cm^{-3} $Hz^{-1/2}$. Under the typical sampling rate of 2.5 and 1 MHz bandwidth, the NEC of HO_2 was ~7.3×10^{10} molecules cm^{-3} (40 shots).

2.4.2. MIR Calibration. The MIR laser monitored OH radicals by probing the fundamental vibrational transition (ν_1,$P(3.5)f$: 3407.6 cm^{-1}, $\sigma_{OH} \sim 2 \times 10^{-18}$ cm^2).[33] This line corresponds to one of two doublets; Figure 5 shows the spectrum of the two OH lines obtained by scanning the optical frequency of the laser and measuring the 2f signal from the reaction of HO_2 with NO. Within experimental uncertainty, HO_2 + NO produces OH with a yield of unity. The line centered at 3407.6 cm^{-1} was chosen, which is free from interferences by HO_2 and H_2O.

The laser signal was calibrated by titrating HO_2 with NO and measuring the kinetics traces of HO_2 and OH from the reaction of HO_2 + NO (Figure 4b) immediately after the HO_2 self-reaction calibration runs. Since the rate constant of this reaction is well-known and all the loss processes of OH are well-characterized, the absolute OH concentration could be determined from the formation and subsequent decay of the OH signal, provided that the initial radical concentrations are known. The initial radical concentrations were assumed to be the same as the HO_2 calibration runs since the same Cl_2 concentrations and excimer energy were used. The OH decays rapidly from reaction with NO and with CH_3OH; therefore, the two lowest initial radical concentrations were used for the HO_2 + NO calibrations in order to accurately capture the peak of the OH signal. The HO_2 and OH decays were simultaneously fit with a kinetics model using FACSIMILE[32] to determine calibration factor, $V_{M,OH}$, which scales the OH laser signal (S_{OH}) to absolute OH concentrations:

$$[OH] = S_{OH} \times V_{M,OH} \quad (4)$$

The NEC $Hz^{-1/2}$ of OH normalized to one excimer shot was 5.0×10^8 molecules cm^{-3} $Hz^{-1/2}$. Under the typical sampling rate of

DOI: 10.1021/acs.jpca.9b00442
J. Phys. Chem. A 2019, 123, 3655−3671

2.5 and 1 MHz bandwidth, the NEC of OH was 6.7×10^9 molecules cm^{-3} (75 shots). It should be noted that further improvement in the OH sensitivity is attainable in future work using the IRKS apparatus. Due to limited MIR reflectivity of the coatings on the Herriott mirrors, maximum sensitivity was not yet realized; thus, optimization of the optics is expected to significantly lower the detection limit of the MIR probe.

The uncertainties in the calibration factors for each laser were determined from Monte Carlo analysis (see Error Analysis). The estimated systematic errors of V_{M,HO_2} and $V_{M,OH}$ were ~10% and 15%, respectively.

3. RESULTS

3.1. Overview. Experiments were carried out at a total pressure of P = 100 Torr at seven temperatures in the range T = 230−294 K. At each temperature, data were collected under 10−15 different experimental conditions that varied in precursor and radical concentrations. For each experimental condition, we averaged 40 excimer laser shots probing in the NIR and λ = 250 nm, and 75 shots probing in the MIR and λ = 225 nm.

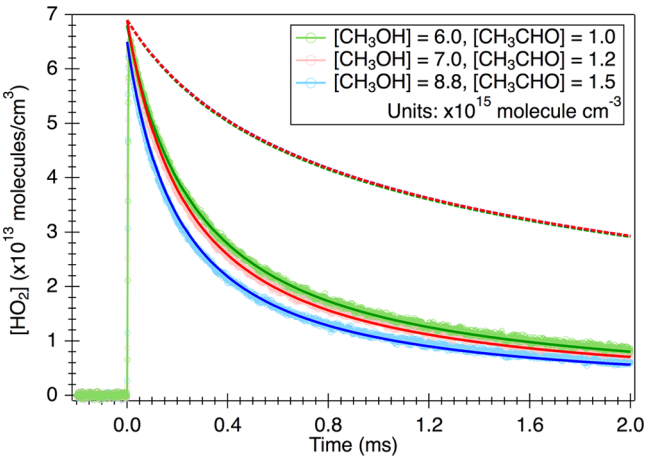

Figure 6. Three HO_2 (NIR) decay curves at various concentrations of CH_3OH and CH_3CHO (fixed $[CH_3OH]$:$[CH_3CHO]$ = 6 and $[Cl]_0$ = 8.7×10^{13} molecules cm^{-3}) at T = 230 K. Data (circle markers) shown with modeled HO_2 profiles: with (solid lines) and without (dashed lines) enhancement effects by CH_3OH and CH_3CHO.

Photolysis of Cl_2 generated Cl atoms (R2):

$$Cl_2 + h\nu\ (351\ nm) \rightarrow 2Cl \qquad (R2)$$

In the presence of O_2, the reaction of the Cl atoms with excess amounts of CH_3OH and CH_3CHO rapidly (<20 μs) produced HO_2 (reactions R3 and R4) and $CH_3C(O)O_2$ (reactions R5 and R6a) with yields very close to unity.

$$Cl + CH_3OH \rightarrow CH_2OH + HCl \qquad (R3)$$

$$CH_2OH + O_2 \rightarrow HO_2 + CH_2O \qquad (R4)$$

$$Cl + CH_3CHO \rightarrow CH_3C(O) + HCl \qquad (R5)$$

$$CH_3C(O) + O_2 \xrightarrow{M} CH_3C(O)O_2 \qquad (R6a)$$

$$\rightarrow OH + C_2H_2O_2 \qquad (R6b)$$

$$\rightarrow HO_2 + CH_2CO \qquad (R6c)$$

The yields of OH and HO_2 from (R6) (α_{6b} and α_{6c}, respectively) were determined from prompt OH and HO_2 formed in the absence of CH_3OH and were found to be ~2−3% at 100 Torr in N_2 across the entire temperature range. (R6a), (R6b), and (R6c) occurred on a much shorter time scale compared to the HO_2 + $CH_3C(O)O_2$ reaction; thus, determination of α_{6b} and α_{6c} was not affected by HO_2 + $CH_3C(O)O_2$ chemistry. One advantage of our direct IR detection technique over the previous LIF experiments was the ability to decouple the OH produced via (R6b) from the OH produced via (R1c). Specifically, the detection sensitivity was not affected by the presence of CH_3OH (and therefore HO_2). Detailed results on (R6) has been reported previously.[34]

We varied the ratio of the initial concentrations of HO_2 and $CH_3C(O)O_2$ ($[HO_2]_0/[CH_3C(O)O_2]_0$) over a wide range, as well as the total initial radical concentration, $[Cl]_0$, to minimize systematic errors introduced by unknown or poorly characterized secondary reactions. A summary of all experimental conditions is given in Tables S1−S8 in the Supporting Information.

$[Cl]_0$ was determined from the NIR measurement of HO_2 formed via (R9) and (R10) in the absence of CH_3CHO. With the addition of CH_3CHO, $[HO_2]_0$ and $[CH_3C(O)O_2]_0$ were determined from the fraction of Cl atoms reacting with the corresponding radical precursors; i.e.,

$$[HO_2]_0 = \frac{k_3[CH_3OH]}{k_3[CH_3OH] + k_5[CH_3CHO]}[Cl]_0 \qquad (5)$$

$$[CH_3C(O)O_2]_0 = \frac{k_5[CH_3CHO]}{k_5[CH_3OH] + k_3[CH_3CHO]}[Cl]_0 \qquad (6)$$

$[HO_2]_0/[CH_3C(O)O_2]_0$ ratios were varied by changing the precursor concentrations. The temperature dependences of k_3 and k_5 in the 230−294 K temperature range have been measured using this apparatus and details will be reported in a separate publication.[35] Briefly, both k_3 and k_5 were found to be temperature-independent, with values of $(5.5 \pm 0.4) \times 10^{-11}$ and $(8.0 \pm 1.3) \times 10^{-11}$ cm^3 $molecule^{-1}$ s^{-1} (2σ uncertainties), respectively, which are consistent with the values recommended by the current JPL and IUPAC databases.

The permissible concentrations of CH_3OH and CH_3CHO were limited by the formation of complexes. At lower temperatures, HO_2 forms hydrogen-bonded adducts with CH_3OH and CH_3CHO. Rapid equilibrium is established (<50 μs) between HO_2 and the adducts, $HO_2{\cdot}CH_3OH$ and $HO_2{\cdot}CH_3CHO$. The $[HO_2]_0$ measured by the high-resolution NIR probe represents only the free, unbound HO_2, because the NIR probes the overtone rovibrational transition of the O−H stretch. Furthermore, the adducts enhance the rate of the HO_2 self-reaction. Experiments were conducted using low $[CH_3OH]$ and $[CH_3CHO]$ to minimize these effects; however, rate enhancement and fast loss of HO_2 could not be completely avoided, especially at lower temperatures. Adduct concentrations could be as high as 25% of $[HO_2]_0$. The impact of the adducts on the kinetics were therefore investigated by varying $[CH_3OH]$ and $[CH_3CHO]$. More details on characterizing the effects of the HO_2 adducts on the overall kinetics of (R1) will be described below.

The range of $[HO_2]_0/[CH_3C(O)O_2]_0$ over which data were collected was limited by the need to minimize competing secondary chemistry. Since k_5 is larger than k_3, $[CH_3OH]$ had to

DOI: 10.1021/acs.jpca.9b00442
J. Phys. Chem. A 2019, 123, 3655−3671

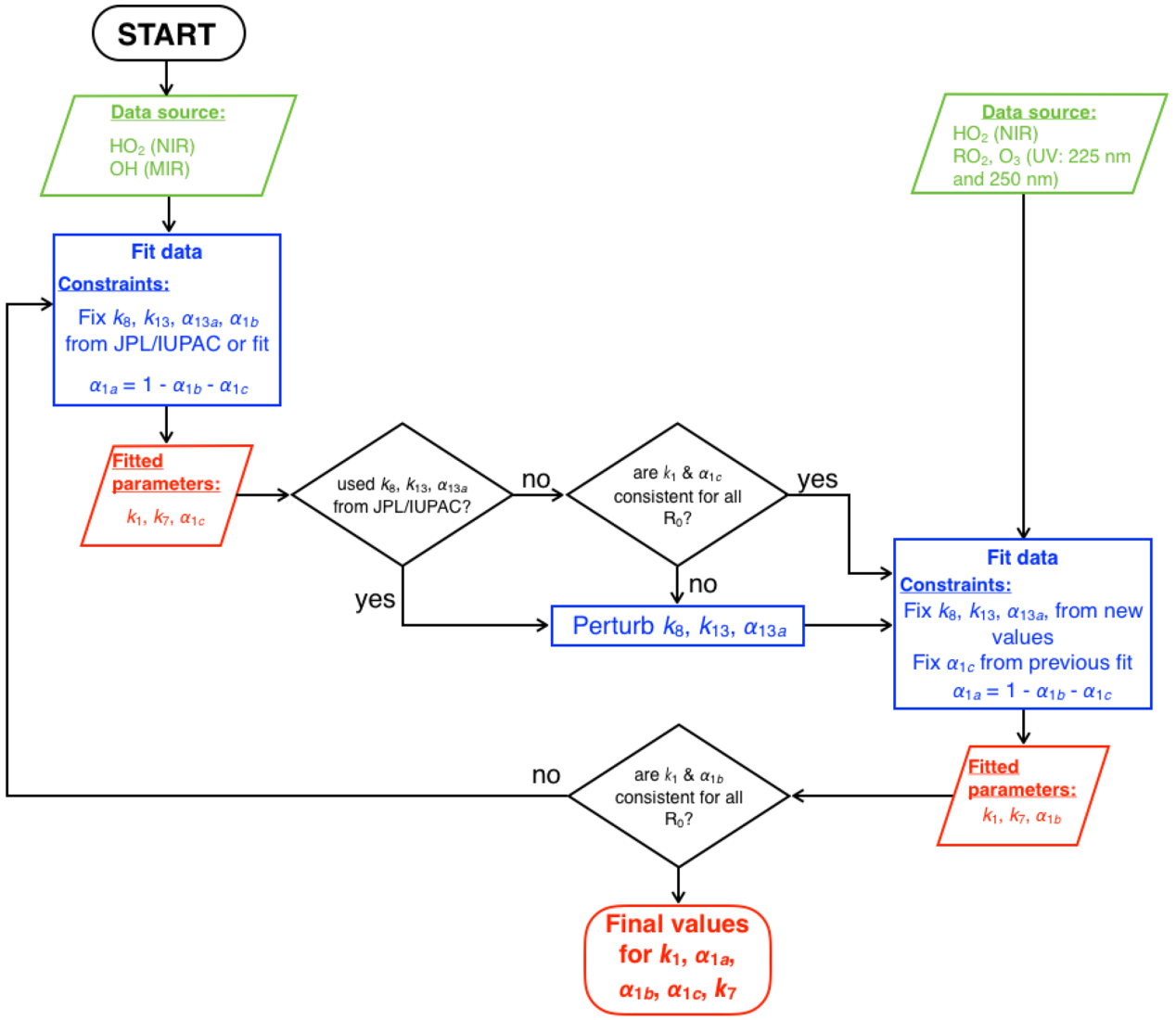

Figure 7. Summary of fitting procedure for determination of k_1, k_7, α_{1a}, α_{1b}, and α_{1c}. $R_0 = [HO_2]_0/[CH_3C(O)O_2]_0$. Fits are done with rate parameters k_8, k_{13}, and α_{13a} for the secondary reactions either fixed to the JPL or IUPAC recommended values or to values determined empirically.

be greater than $[CH_3CHO]$ to ensure that enough HO_2 radicals were generated such that the $CH_3C(O)O_2$ self-reaction did not dominate. However, $[CH_3OH]$ also had to be sufficiently low to minimize the subsequent loss of HO_2 with the adducts formed with CH_3OH and CH_3CHO, which in turn limited the range of $[CH_3CHO]$ that could be used. The $[Cl]_0$ was constrained as well. It was kept low to minimize secondary loss processes, but had to be high enough to obtain detectable yields of OH.

3.2. Analysis. Competing fast radical recycling and secondary chemistry precluded the analysis of (R1) using a conventional first-order treatment. Therefore, data analysis required the use of a kinetics model to account for all major radical loss and recycling processes. In addition to accounting for the formation chemistry for $CH_3C(O)O_2$ and HO_2 radicals and their mutual reaction, the kinetics model also had to consider the secondary reactions of $CH_3C(O)O_2$ and the effect of weakly bound HO_2 complexes on the self-reaction of HO_2. The impact of these processes on the determination of the rate constants and branching yields for (R1) is discussed below. In this section we will discuss the effects of secondary chemistry and HO_2 chaperone chemistry in subsections 3.2.1 and 3.2.2. In subsection 3.2.3 we will describe the method for determination of the overall rate coefficient and branching yields for (R1). The error analysis approach will be described in subsection 3.2.4.

3.2.1. Secondary $CH_3C(O)O_2$ Chemistry. In the laboratory, measurements of the kinetic rate constant k_1, even at short time scales, are complicated by the self-reactions of $CH_3C(O)O_2$ and HO_2 that compete with (R1):

$$HO_2 + HO_2 \xrightarrow{M} H_2O_2 + O_2 \quad \text{(R7)}$$

$$CH_3C(O)O_2 + CH_3C(O)O_2 \rightarrow 2CH_3C(O)O + O_2 \quad \text{(R8)}$$

The competition of (R1), (R7), and (R8), and the subsequent reactions of $CH_3C(O)O$ produced from (R1c) and (R8) preclude pseudo-first-order kinetics experiments, consequently preventing analytical solutions to the rate equations. For example, $CH_3C(O)O$ from (R1c) and (R8) rapidly decomposes (assumed instantaneous) to form CH_3, which produces CH_3O_2 upon addition of O_2:

$$CH_3C(O)O \xrightarrow{M} CH_3 + CO_2 \quad \text{(R9)}$$

$$CH_3 + O_2 \xrightarrow{M} CH_3O_2 \quad \text{(R10)}$$

DOI: 10.1021/acs.jpca.9b00442
J. Phys. Chem. A 2019, 123, 3655−3671

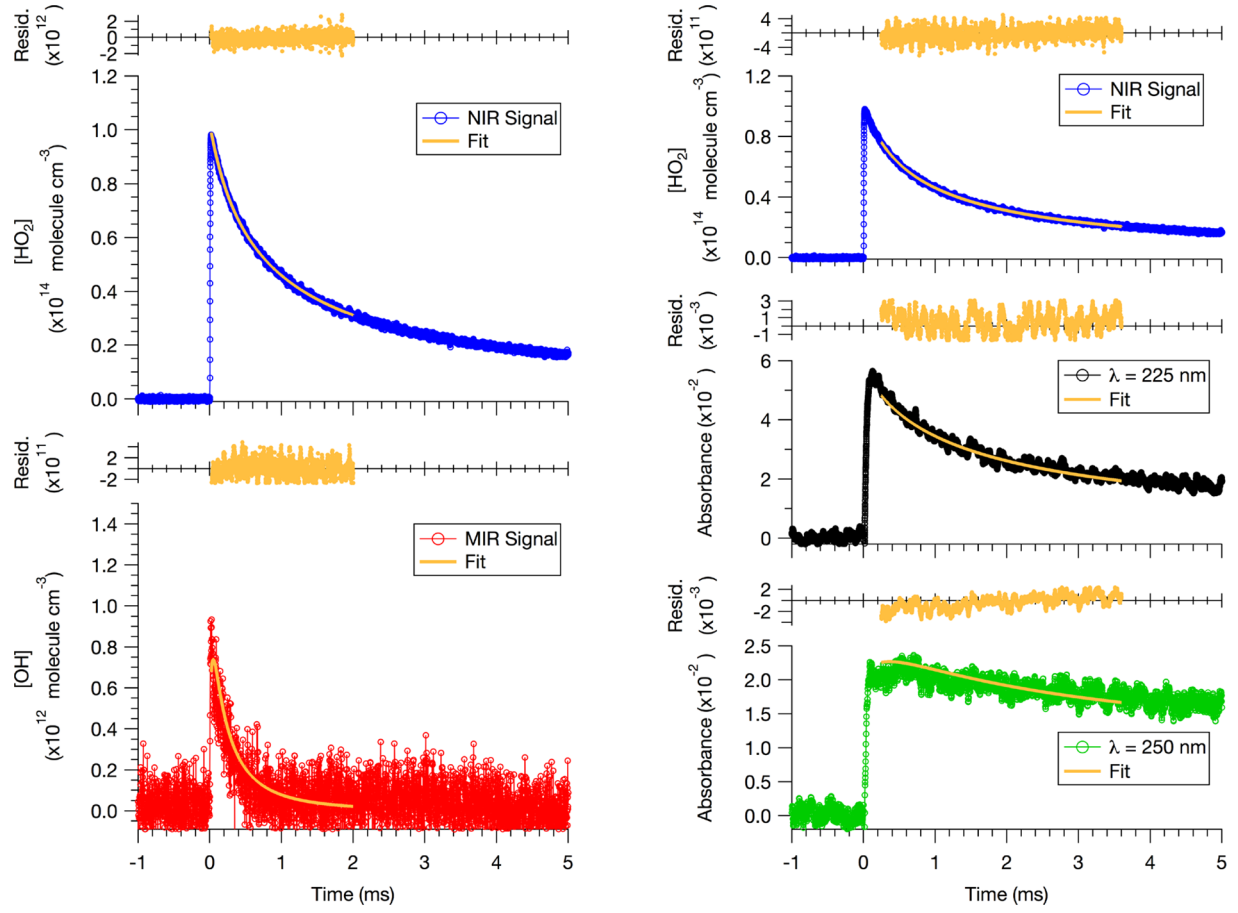

Figure 8. Fits (orange) to NIR (blue), MIR (red), and UV (black and green) data from the $HO_2 + CH_3C(O)O_2$ reaction, collected at $T = 260$ K and $P = 100$ Torr: (a) NIR HO_2 and MIR OH signals fitted from 0.02 to 1 ms and (b) NIR HO_2 and UV signals (black, $\lambda = 225$ nm; green, $\lambda = 250$ nm) fitted from 0.2 to 3.6 ms. Residuals to fits are shown above each curve. Precursor and radical concentrations: $[Cl_2] = 3.8 \times 10^{15}$ molecules cm^{-3}; $[CH_3OH] = 5.0 \times 10^{15}$ molecules cm^{-3}; $[CH_3CHO] = 1.0 \times 10^{15}$ molecules cm^{-3}; $[Cl]_0 = 1.2 \times 10^{14}$ molecules cm^{-3}.

Table 3. Summary of Experimental Conditions and Results[a]

T (K)	$[CH_3OH]$ ($\times 10^{15}$ cm^{-3})	$[CH_3CHO]$ ($\times 10^{15}$ cm^{-3})	$[Cl]_0$ ($\times 10^{15}$ cm^{-3})	$[HO_2]_0/[CH_3C(O)O_2]_0$	k_1 ($\times 10^{-11}$ cm^3 s^{-1})	α_{1a}	α_{1b}	α_{1c}
294.0	2.0–6.0	1.0	5.9–9.3	1.3–4.0	1.72 ± 0.22	0.29 ± 0.12	0.23 ± 0.07	0.48 ± 0.09
292.7	5.0–8.8	1.0–2.3	8.3	2.1–4.8	1.75 ± 0.19	0.33 ± 0.10	0.22 ± 0.06	0.45 ± 0.07
280.1	4.0–8.8	1.0–2.2	13	2.7–4.7	1.77 ± 0.19	0.30 ± 0.10	0.25 ± 0.07	0.44 ± 0.07
270.6	4.0–8.8	1.0–2.2	13	2.7–4.8	1.91 ± 0.20	0.32 ± 0.10	0.28 ± 0.08	0.40 ± 0.07
259.3	3.0–8.8	1.0–2.9	11–13	2.0–4.8	2.33 ± 0.34	0.30 ± 0.12	0.31 ± 0.08	0.39 ± 0.08
250.4	3.0–8.8	1.0–2.3	6.8–8.3	2.0–4.7	2.67 ± 0.24	0.25 ± 0.15	0.40 ± 0.13	0.35 ± 0.08
240.1	3.0–8.8	1.0–2.2	5.7–9.1	2.1–4.8	2.84 ± 0.65	0.26 ± 0.16	0.42 ± 0.13	0.32 ± 0.09
228.9	3.0–8.8	1.0–2.3	5.6–8.7	2.1–4.7	3.63 ± 1.11	0.26 ± 0.13	0.45 ± 0.12	0.29 ± 0.05

[a]All experiments were conducted at a total pressure of 100 Torr in N_2 buffer gas.

Reactions of CH_3 other than (R10) were also considered (e.g., $CH_3 + RO_2$ and $CH_3 + CH_3$) but were found to be negligible under our experimental conditions where we have a large excess of O_2 relative to both HO_2 and RO_2. CH_3O_2 subsequently undergoes self-reaction via (R11) as well as cross-reactions with HO_2 (R12) and with $CH_3C(O)O_2$ (R13):

$$CH_3O_2 + CH_3O_2 \rightarrow 2CH_3O + O_2 \quad \text{(R11a)}$$

$$\rightarrow CH_3OH + CH_2O + O_2 \quad \text{(R11b)}$$

$$HO_2 + CH_3O_2 \rightarrow CH_3OOH + O_2 \quad \text{(R12a)}$$

$$\rightarrow CH_2O + H_2O + O_2 \quad \text{(R12b)}$$

$$CH_3O_2 + CH_3C(O)O_2 \rightarrow CH_3C(O)O + CH_3O + O_2 \quad \text{(R13a)}$$

$$\rightarrow CH_3C(O)OH + CH_2O + O_2 \quad \text{(R13b)}$$

Under conditions where O_2 is in excess, CH_3O from (R13a) and (R11a) generates secondary HO_2:

$$CH_3O + O_2 \rightarrow HO_2 + CH_2O \quad \text{(R14)}$$

DOI: 10.1021/acs.jpca.9b00442
J. Phys. Chem. A 2019, 123, 3655−3671

Table 4. Full List of Reactions and Rate Constants Used in the Kinetics Model

	reaction		rate constant ($cm^3\ s^{-1}$)	ref
		Methanol		
(R3)	$Cl + CH_3OH$	$\rightarrow CH_2OH + HCl$	5.5×10^{-11}	29, 35
(R18a)	$OH + CH_3OH$	$\rightarrow CH_2OH + H_2O$	$0.85 \times 2.90 \times 10^{-12} \exp(345/T)$	29
(R18b)		$\rightarrow CH_3OH + H_2O$	$0.15 \times 2.90 \times 10^{-12} \exp(345/T)$	29
(R4)	$CH_2OH + O_2$	$\rightarrow HO_2 + CH_2O$	9.1×10^{-11}	29
		Acetaldehyde		
(R5)	$Cl + CH_3CHO$	$\rightarrow CH_3CO + HCl$	8.0×10^{-11}	35, 43
(R19a)	$OH + CH_3CHO$	$\rightarrow CH_3CO + H_2O$	$0.95 \times 4.63 \times 10^{-12} \exp(350/T)$	29
(R19b)		$\rightarrow CH_2CHO + H_2O$	$0.05 \times 4.63 \times 10^{-12} \exp(350/T)$	29
(R6a)	$CH_3C(O) + O_2$	$\rightarrow CH_3C(O)O_2$	$(1 - \alpha_{6b} - \alpha_{6c}) \times 5.1 \times 10^{-12}$	overall rate constant:[43]
(R6b)		$\rightarrow OH + products$	$\alpha_{6b} \times 5.1 \times 10^{-12}$	branching yields[34]
(R6c)		$\rightarrow HO_2 + products$	$\alpha_{6c} \times 5.1 \times 10^{-12}$	
		HO_x Reactions		
(R7)	$HO_2 + HO_2$	$\xrightarrow{M} H_2O_2 + O_2$	k_7	varied, see text
(R20)	$OH + HO_2$	$\rightarrow H_2O + O_2$	$4.8 \times 10^{-11} \exp(250/T)$	29
(R21a)	$OH + OH$	$\rightarrow H_2O + O$	1.8×10^{-12}	29
(R21b)	$OH + OH$	$\xrightarrow{M} H_2O_2$	$k_0 = 6.9 \times 10^{-31}(300/T)^{-1.0}$	29
			$k_\infty = 2.6 \times 10^{-11}$	29
(R22)	$OH + H_2O_2$	$\rightarrow H_2O + HO_2$	1.8×10^{-12}	29
(R23)	$OH + CH_2O$	$\rightarrow H_2O + HCO$	$5.5 \times 10^{-12} \exp(125/T)$	29
(R24)	$HCO + O_2$	$\rightarrow HO_2 + CO$	5.2×10^{-12}	29
(R25)	$O + OH$	$\rightarrow O_2 + H$	$1.8 \times 10^{-11} \exp(180/T)$	29
(R26)	$O + HO_2$	$\rightarrow O_2 + OH$	$3.0 \times 10^{-11} \exp(200/T)$	29
(R27)	$H + O_2$	$\xrightarrow{M} HO_2$	$k_0 = 4.4 \times 10^{-32}(300/T)^{-1.3}$	
			$k_\infty = 7.5 \times 10^{-11}(300/T)^{0.2}$	
(R28)	$HO + O_3$	$OH + O_3 \rightarrow HO_2 + O_2$	$1.7 \times 10^{-12} \exp(-940/T)$	29
(R29)	$HO_2 + O_3$	$\rightarrow OH + 2O_2$	$1.0 \times 10^{-14} \exp(-490/T)$	29
		RO_2 Reactions		
(R1a)	$HO_2 + CH_3C(O)O_2$	$\rightarrow CH_3C(O)OOH + O_2$	$(1 - \alpha_{1b} - v\alpha_{1b}) \times k_1$	varied, this work
(R1b)		$\rightarrow CH_3C(O)OH + O_3$	$\alpha_{1b} \times k_1$	varied, this work
(R1c)		$\rightarrow OH + CH_3C(O)O + O_2$	$\alpha_{1c} \times k_1$	varied, this work
(R12a)	$HO_2 + CH_3O_2$	$\rightarrow CH_3OOH + O_2$	$\{1-1/[1 + 498\exp(-1160/T)]\} \times 3.8 \times 10^{-13} \exp(780/T)$	29
(R12b)		$\rightarrow CH_2O + H_2O + O_2$	$\{1/[1 + 498\exp(-1160/T)]\} \times 3.8 \times 10^{-13} \exp(780/T)$	
(R8)	$2CH_3C(O)O_2$	$\rightarrow 2CH_3C(O)O + O_2$	k_8	varied, see text
(R13a)	$CH_3O_2 + CH_3C(O)O_2$	$\rightarrow CH_3C(O)O + CH_3O + O_2$	$\alpha_{13a} \times k_{13}$	varied, see text
(R13b)		$\rightarrow CH_3C(O)OH + CH_2O + O_2$	$(1 - \alpha_{13a}) \times k_{13}$	varied, see text
(R11a)	$CH_3O_2 + CH_3O_2$	$\rightarrow 2CH_3O + O_2$	$\{1-1/[1 + 26.2\exp(-1130/T)]\} \times 9.5 \times 10^{-14} \exp(390/T)$	29
(R11b)		$\rightarrow CH_3OH + CH_2O + O_2$	$\{1/[1 + 26.2\exp(-1130/T)]\} \times 9.5 \times 10^{-14} \exp(390/T)$	
(R14)	$CH_3O + O_2$	$\rightarrow CH_2O + HO_2$	$3.9 \times 10^{-14} \exp(-900/T)$	29
(R9)	$CH_3C(O)O$	$\rightarrow CH_3 + CO_2$	assumed instantaneous	29
(R10)	$CH_3 + O_2$	$\xrightarrow{M} CH_3O_2$	$k_0 = 4.0 \times 10^{-31}(300/T)^{-3.6}$	29
			$k_\infty = 1.2 \times 10^{-12}(300/T)^{1.1}$	

Thus, characterization of (R1) relies heavily on the accuracy of the kinetics of the secondary chemistry. Some of the main challenges in the data analysis originated from systematic errors associated with (R8) and (R13), which have only been investigated by a small number of experimental studies,[19,36−38] none of which have accounted for the OH product channel from (R1). The current recommendations from the IUPAC and JPL[29] data evaluations are based on analogous reactions due to the limited number of temperature dependence studies of (R8) and (R13). As part of this work, we also carried out additional experiments in the absence of CH_3OH, where no HO_2 was initially formed, in order to characterize (R8) and (R13). However, unique solutions for k_8, k_{13}, and α_{13a} could not be determined from these experiments due to poorly constrained fits.

Our approach to indirectly estimate k_8, k_{13}, and α_{13a} consisted of iteratively fitting data with various $[HO_2]_0/[CH_3C(O)O_2]_0$ ratios. A diagram summarizing the fitting procedure (Figure 7) is provided in section 3.2.3. In the first iteration, only the data sets with the highest $[HO_2]_0/[CH_3C(O)O_2]_0$ ratios (~3.5−5) were used, constraining k_1, α_{1b}, and α_{1c}, while fixing the values of k_8, k_{13}, and α_{13a} to the recommended values from the current JPL data evaluation.[29] Next, sensitivity of the data to (R8), (R13a), and (R13b) was explored by adjusting the values of k_8, k_{13}, and α_{13a} independently by ±20%. For data sets with high $[HO_2]_0/[CH_3C(O)O_2]_0$, the fitted values of k_1, α_{1b}, and α_{1c} did not vary

DOI: 10.1021/acs.jpca.9b00442
J. Phys. Chem. A 2019, 123, 3655−3671

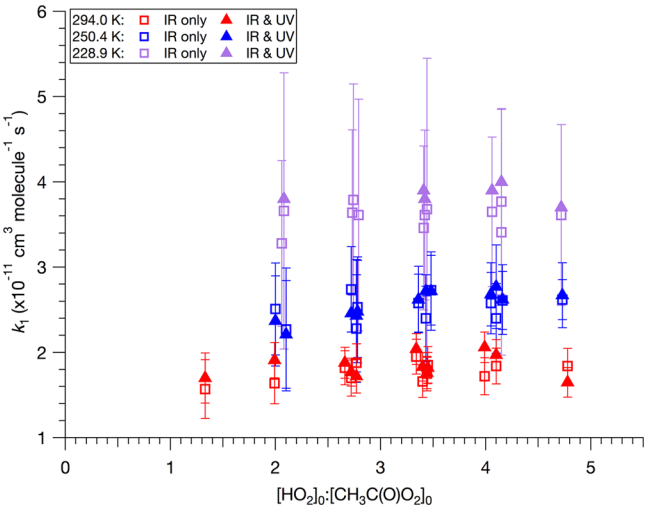

Figure 9. Fitted values of k_1 plotted as a function of $[HO_2]_0/[CH_3C(O)O_2]_0$, shown for three temperatures: 228.9 K (purple), 250.4 K (blue), and 294.0 K (red); data from other temperatures were excluded for clarity. Values determined from the NIR and MIR fits (squares) agree with those determined from the NIR and UV fits (triangles).

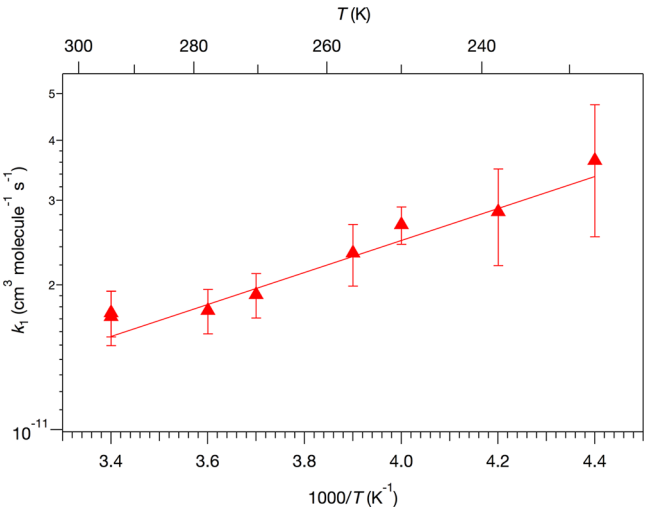

Figure 10. Arrhenius plot of the overall rate constant, k_1.

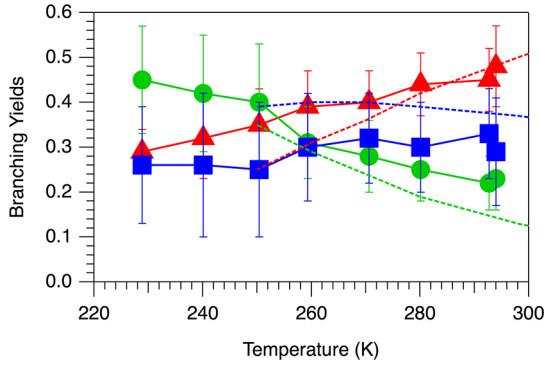

Figure 11. Measured temperature dependence of α_{1a} (blue squares), α_{1b} (green circles), and α_{1c} (red triangles). IUPAC recommendations over their applicable temperature ranges are shown in the dashed lines.

by more than ±20%, confirming that these data sets were not sensitive to (R8) and (R13). Data sets with lower $[HO_2]_0/[CH_3C(O)O_2]_0$ ratios were found to be more sensitive to these parameters; thus, k_8, k_{13}, and α_{13a} had to be adjusted until the fitted values of k_1, α_{1c}, and α_{1b} from all data sets converged.

The estimated values of k_8 and k_{13} determined in this fitting procedure are well within the error bands of the current JPL data evaluation[29] and are provided in the Supporting Information (Figure S1). Values of α_{13a} ranging between 1.0 to 0.9 were also found to provide the best fits to the data across all temperatures studied. k_8, k_{13}, and α_{13a} were highly correlated with other parameters; thus, the measured values are not unique solutions and should not be interpreted as direct measurements. Rather, these kinetics parameters were determined empirically; we used values that were consistent with those in the literature (within the 95% uncertainty bounds), as well as with our data under all experimental conditions. These values of k_8, k_{13}, and α_{13a} were then used to repeat the fits to all data sets, although results from the high $[HO_2]_0/[CH_3C(O)O_2]_0$ data were not significantly affected.

In addition to the secondary reactions described above, the loss of OH via reaction with CH_3O_2 and with $CH_3C(O)O_2$ were also considered in the data analysis. However, inclusion of these reactions (using an estimated value of 1×10^{-10} cm^3 molecule^{-1} s^{-1} for the rate constants[39]) in our kinetics models did not make a noticeable difference in our inferred values of α_{1c}. Since $[CH_3CHO]$ was greatly in excess of $[CH_3O_2]$ and $[CH_3C(O)O_2]$ by approximately a factor of 40 or more, the OH loss was dominated by reaction with CH_3CHO.

3.2.2. Impact of HO_2 + HO_2 Rate Enhancement by Radical Adducts on k_1. An additional complication is introduced at lower temperatures, where HO_2 forms a hydrogen-bonded adduct with the radical precursors:[20,21,23,24,40,41]

$$HO_2 + X \overset{[M]}{\rightleftharpoons} HO_2{\cdot}X \qquad \text{(R15)}$$

where X = CH_3OH or CH_3CHO. Adduct formation impacts the data analysis in several ways: (1) rapid loss of HO_2 via (R15) influences determination of $[HO_2]_0$; (2) the apparent HO_2 self-reaction rate constant is enhanced due to the additional loss of HO_2 by reaction with $HO_2{\cdot}X$. In the case of CH_3CHO, ab initio calculations suggest rapid isomerization of the initially formed $HO_2{\cdot}CH_3CHO$ adduct to the α-hydroxyethylperoxy radical ($CH_3CH(OH)O_2$),[42] which can also react with HO_2. As we will discuss below, details of this process are unimportant for the present work because we define an effective rate constant that accounts for the additional HO_2 loss pathway.

First, adduct formation led to a lower observed peak concentration of HO_2. $[Cl]_0$ at each temperature was typically determined by measuring the decay of HO_2 in the absence of CH_3CHO; i.e.,

$$[Cl]_0 = [HO_2]_0 \qquad (7)$$

The data were fit with a simple bimolecular reaction and extrapolated to $t = 0$ to obtain $[HO_2]_0$. For a fixed $[Cl_2]$ and excimer energy, the measured $[HO_2]_0$ for $T > 250$ K was equal to the $[HO_2]_0$ determined at room temperature. However, measurements at $T \leq 250$ K underdetermined $[HO_2]_0$ due to the rapid loss of HO_2 via (R15) (X = CH_3OH), which was not captured by the kinetics model. $[Cl]_0$ is described by eq 8:

$$[Cl]_0 = [HO_2]_{eq} + [HO_2{\cdot}X]_{eq} \qquad (8)$$

where $[HO_2]_{eq}$ and $[HO_2{\cdot}X]_{eq}$ are the equilibrium concentrations of HO_2 and $HO_2{\cdot}X$. The NIR detection of HO_2 selectively detected the free HO_2, and not $HO_2{\cdot}X$, i.e., the

DOI: 10.1021/acs.jpca.9b00442
J. Phys. Chem. A 2019, 123, 3655−3671

Table 5. Parameters varied in Monte Carlo simulations. All uncertainties are 1σ

parameter	standard dev	ref
$[Cl]_0$ (molecules cm^{-3})	$0.1[Cl]_0$	*a*
UV path length (cm)	10	34, 44
V_{M,HO_2} (molecules cm^{-3} mV^{-1})	$0.1V_{M,HO_2}$	*a*
$V_{M,OH}$ (molecules cm^{-3} mV^{-1})	$0.15V_{M,OH}$	*a*
k_8 (cm^3 molecule^{-1} s^{-1})	$\left(1.5\exp\left(\left\lvert 150\left(\frac{1.0}{T}-\frac{1.0}{298}\right)\right\rvert\right)-1\right)k_8$	JPL 15−10[29]
k_{13} (cm^3 molecule^{-1} s^{-1})	$\left(1.5\exp\left(\left\lvert 250\left(\frac{1.0}{T}-\frac{1.0}{298}\right)\right\rvert\right)-1\right)k_{13}$	JPL 15−10[29]
α_{13a}	0.1	
UV absorption cross sections	see Table 2	

[a]Uncertainties from Monte Carlo fits.

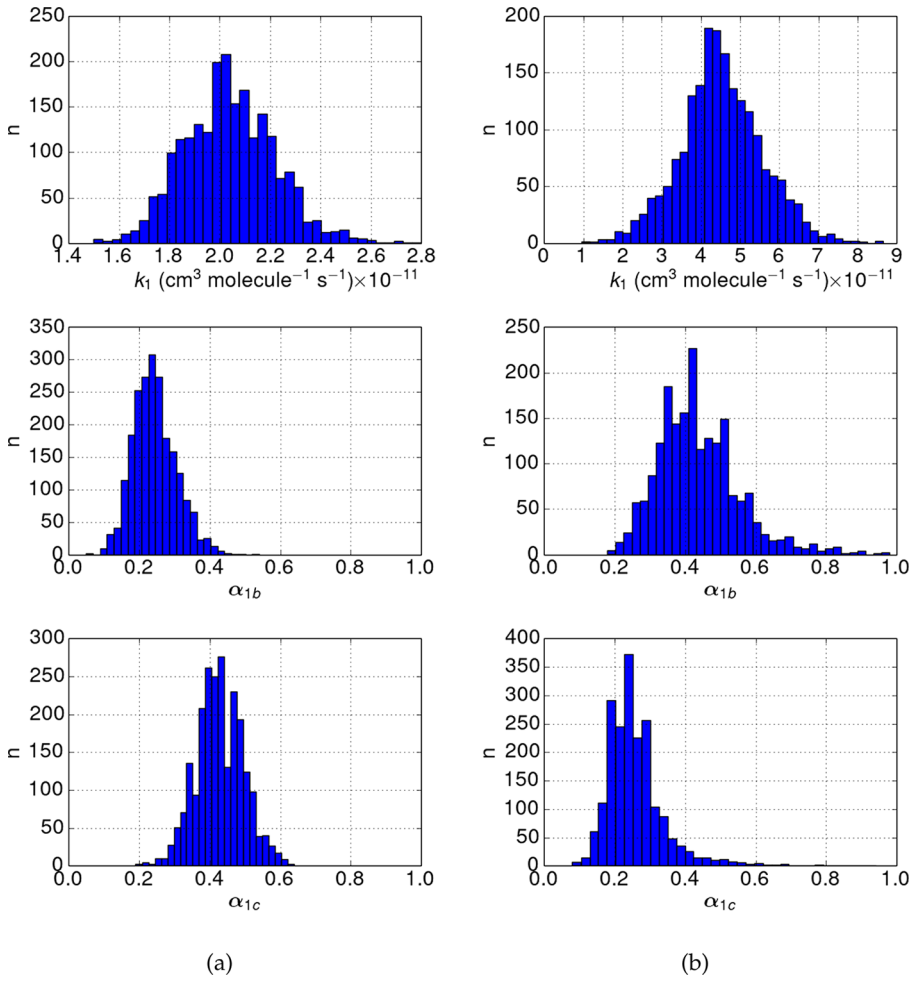

Figure 12. Histograms of k_1, α_{1b}, and α_{1c} of data collected at (a) T = 294 K and (b) T = 230 K. Total number of simulations = 2000. P = 100 Torr. Concentrations: $[Cl]_0 = 8.8 \times 10^{13}$ molecules cm^{-3}; $[CH_3OH] = 5.0 \times 10^{15}$ molecules cm^{-3}; $[CH_3CHO] = 1.0 \times 10^{15}$ molecules cm^{-3}.

concentration of HO_2 extrapolated to $t = 0$ is $[HO_2]_{eq}$. However, the UV signal presumably includes absorbance by both HO_2 and $HO_2{\cdot}X$; therefore, $[HO_2]_0$ for the UV curves was always constrained to the value determined from the room temperature HO_2 self-reaction data, which was collected at the same $[Cl_2]$ and excimer energy. Fits to the NIR curves included an additional parameter, $[HO_2]_{eq}$. Although the equilibrium constants of (R15) for CH_3OH[22] and CH_3CHO[34] have been measured previously, $[HO_2]_{eq}$ was allowed to be an additional fitted parameter in these fits. $[HO_2{\cdot}X]_{eq}$ agreed within experimental error to the calculated value using the measured equilibrium constants. At the highest $[CH_3OH]$ and $[CH_3CHO]$ used, the fraction of total HO_2 bound as an adduct (i.e., $([HO_2{\cdot}CH_3OH] + [HO_2{\cdot}CH_3CHO])/[HO_2]_0$) was ∼25% at 230 K and ∼2% at 294 K.

Second, (R15) affects the kinetics because the effective rate constant of (R17) is enhanced due to the subsequent reactive losses of the radical adducts.

DOI: 10.1021/acs.jpca.9b00442
J. Phys. Chem. A 2019, 123, 3655−3671

$$HO_2 + HO_2{\cdot}X \rightarrow \text{products} \quad \text{(R16)}$$

$$HO_2{\cdot}X + HO_2{\cdot}X \rightarrow \text{products} \quad \text{(R17)}$$

In the case of X = CH_3OH, the enhanced observed rate constant results from $HO_2{\cdot}CH_3OH$ acting as a chaperone to increase the rate of formation of H_2O_2 and O_2.[23,41] The rate enhancement becomes more significant with the larger $[HO_2{\cdot}X]$ at lower temperatures.[22] Three HO_2 decay curves collected at 230 K using the same initial amount of total radicals are plotted in Figure 6. The concentration of the radical precursors were varied, but the ratio was kept the same; i.e., all three runs had the same relative amount of initial HO_2 to $CH_3C(O)O_2$. In the absence of rate enhancement by the radical precursors, the rate of decay should be identical, as predicted by the model (dashed lines).

In the absence of CH_3CHO, rate enhancement has been described by an effective rate constant, $k''_{7,M}$, with a linear dependence on $[CH_3OH]$, such that the observed second-order rate constant of the HO_2 self-reaction (R7) is expressed as

$$k_{7,obs,M} = k_7 + k''_{7,M}[CH_3OH] \quad (9)$$

where k_7 is the pressure-dependent $HO_2 + HO_2$ rate constant in the limit of $[CH_3OH] = 0$. The effective negative temperature dependence of $k_{7,obs,M}$ is therefore dependent on the temperature dependence of $k''_{7,M}$, which has been measured previously in this lab.

With the addition of CH_3CHO, the observed rate constant of the HO_2 self-reaction was also found to have a linear dependence on $[CH_3CHO]$ and is denoted as $k_{7,obs,A}$. Experiments were conducted using varying $[CH_3CHO]$ for fixed $[CH_3OH]$, and the results demonstrated that $k_{7,obs,A}$ obeyed the expression,

$$k_{7,obs,A} = k_7 + k''_{7,M}[CH_3OH] + k''_{7,A}[CH_3CHO] \quad (10)$$

$k_{7,obs,A}$ extrapolated to $[CH_3CHO] = 0$ was found to be in excellent agreement with $k_{7,obs,M}$ calculated from eq 9. Including a rate enhancement effect by both CH_3OH and CH_3CHO significantly improves the agreement between the data and the model (solid lines in Figure 6). More details on the determination of $k''_{7,A}$ have been reported previously.[34]

3.2.3. Determination of k_1, α_{1a}, α_{1b}, and α_{1c}. Values of k_1, α_{1a}, α_{1b}, and α_{1c} were determined iteratively along with the kinetics parameters of the major secondary reactions as described in sections 3.2.1 and 3.2.2. The fitted values of the rate constants and branching yields were self-consistent across all experimental conditions. The approach for obtaining the best-fit values of k_1, α_{1a}, α_{1b}, and α_{1c} is described below and shown diagrammatically in Figure 7.

The NIR and MIR curves were simultaneously fitted from ~20 μs to ~1 ms after the photolysis pulse (Figure 8a) to obtain k_1 and α_{1c}. The data were observed to be insensitive to α_{1b}, which was held fixed to the current literature value. We did not use the UV data, since the UV data in the first ~150 μs after photolysis was lost due to PMT saturation from the scattered excimer pulse. This part of the analysis allowed us to probe the rapid kinetic decay of OH. Due to low OH yields, the MIR signals were small and close to the baseline. However, the baseline of the MIR signal fluctuated, which was caused by electrical noise and imperfect laser beam alignment. Limiting the fitting time range to ~1 ms avoided systematic errors. Fitting only the IR signals had the additional advantage that the NIR and MIR signals provided selective, unambiguous detection of HO_2 and OH radicals, respectively, and were not limited by uncertainties in the absorption cross sections of various species that spectrally overlapped.

The longer time scale chemistry was captured in the second part of the data analysis. The NIR signal and the two UV absorbance signals (225 and 250 nm) were simultaneously fitted from 200 μs to 3.5−6 ms after the photolysis pulse (Figure 8b). At longer kinetics times, absorbance by O_3 dominated the UV signal at λ = 250 nm, enabling the determination of α_{1b}. Plots of relative contributions of the main absorbers to the time-dependent UV traces shown in Figure 8b are provided in the Supporting Information (Figure S1). Both k_1 and α_{1b} were floated, and α_{1c} was fixed to the values determined from the short time scale fits. Since the same NIR data was used in both parts of the analysis procedure, agreement between the fitted values of k_1 determined from the short and the long time scale fits served to verify that the two analysis methods were self-consistent. We typically varied the four kinetics parameters while fixing all other rate parameters and applying the constraint given by eq 2. The χ-squared distribution for each data curve was weighted by the standard errors of regression, which were determined from the root-mean-square of the noise of each curve.

Table 3 lists the weighted averages of k_1, α_{1a}, α_{1b}, and α_{1c} measured from data collected over a wide range of experimental conditions. The values were weighted by uncertainties determined from rigorous error analysis, which will be described in the Error Analysis section. The full list of reactions and rate constants used in the kinetics model is given in Table 4.

Figure 9 shows a plot of the values of k_1 as a function of $[HO_2]_0/[CH_3C(O)O_2]_0$ determined from the two fitting methods, i.e., IR only at short time scales and IR and UV at long time scales. We found that the two methods were self-consistent and that the results were invariant across the entire range of $[HO_2]_0/[CH_3C(O)O_2]_0$. Three temperatures were selected for clarity, but the results were consistent across the entire temperature range studied. Similar plots for all temperatures are provided in the Supporting Information (Figure S2).

Figure 10 shows that k_1 has a negative temperature dependence, which is consistent with previous measurements.[19−21] The larger errors at lower temperatures are attributed to larger uncertainties in the kinetics parameters of secondary reactions. The temperature dependences of α_{1a}, α_{1b}, and α_{1c} are plotted in Figure 11. α_{1a} is relatively temperature-independent over this temperature range, while α_{1b} and α_{1c} are anticorrelated.

3.2.4. Error Analysis. The fitted values of k_1, α_{1a}, α_{1b}, and α_{1c} from all data sets were self-consistent and the random errors were small, with standard errors less than 2%. However, these errors are not representative of the overall error, as they do not include systematic errors in the kinetics model that was used in the data analysis. For example, uncertainties in the rate constants and product yields of (R8) and (R13), as well as uncertainties in the UV absorption cross sections, UV path length, calibration factors, and initial radical concentrations all contribute to systematic error. To assess the impact of these errors, Monte Carlo simulations were performed, repeating the fitting procedure 2000 times for each data set. For each simulation, the values of selected input parameters were randomly generated, assuming that each value had a Gaussian distribution with a given mean value and standard deviation. Values of α_{1b} and α_{1c} were also restricted to lie between 0 and 1. Table 2 and

DOI: 10.1021/acs.jpca.9b00442
J. Phys. Chem. A 2019, 123, 3655−3671

Table 6. Comparison of Previous and Current Results at Room Temperature

ref	T (K)	P (Torr)	k_1 ($\times 10^{-11}$ cm^3 s^{-1})	α_{1a}	α_{1b}	α_{1c}
Niki et al.[10]	298	700		0.75 ± 0.03	0.25 ± 0.03	[a]
Moortgat et al.[19]	298	600−650	1.3 ± 0.3	0.67 ± 0.07	0.33 ± 0.07	[a]
Horie and Moortgat[11]	298	730−770		0.73	0.27	[a]
Crawford et al.[20]	295	50	4.4 ± 1.6	0.88 ± 0.04	0.12 ± 0.04	[a]
Tomas et al.[21]	298	760	1.51 ± 0.07	0.80 ± 0.02	0.20 ± 0.02	[a]
Hasson et al.[9]	298	800		0.40 ± 0.16	0.20 ± 0.08	0.40 ± 0.16
Le Crâne et al.[14]	298	760	1.50 ± 0.08	0.80 ± 0.01	0.20 ± 0.01	<0.1
Jenkin et al.[15]	296	700		0.38 ± 0.13	0.12 ± 0.04	0.43 ± 0.10
Dillon and Crowley[16]	298	75−529	1.4 ± 0.5			0.5 ± 0.2
Groß et al.[17]	298	100−500	2.1 ± 0.4	0.23 ± 0.12	0.16 ± 0.08	0.61 ± 0.09
Winiberg et al.[18]	293	750	2.4 ± 0.4	0.37 ± 0.10	0.12 ± 0.04	0.51 ± 0.12
IUPAC[1]	298		2.2	0.37 ± 0.10	0.13 ± 0.10	0.50 ± 0.10
JPL,[29] Tyndall et al.[30]	298		1.40	0.80	0.20	[a]
this work	294	100	1.72 ± 0.22	0.29 ± 0.12	0.23 ± 0.07	0.48 ± 0.09

[a]Assumed $\alpha_{1c} = 0$.

Table 5 list the input parameters and the range of values over which they were allowed to vary.

Results from the Monte Carlo simulations were used to generate histograms of k_1, α_{1b}, and α_{1c}. The frequency distributions of the fitted values of k_1, α_{1b}, and α_{1c} for data sets from T = 294 K and T = 230 K are shown in Figure 12a and Figure 12b, respectively. Histograms generated from each experimental run were each fit with a Gaussian function, and the overall 1σ uncertainties for these parameters were taken from the single standard deviations of the Gaussian distributions. The uncertainties determined from the Monte Carlo simulations varied in magnitude depending on the experimental conditions. For example, experiments conducted under low $[HO_2]_0/[CH_3C(O)O_2]_0$ conditions were more affected by errors in k_8, k_{13}, and α_{13a} compared to high $[HO_2]_0/[CH_3C(O)O_2]_0$ experiments due to the higher prevalence of the secondary reactions of $CH_3C(O)O_2$. The final values and uncertainties of k_1, α_{1b}, and α_{1c} at each temperature were determined by taking the weighted average of results obtained from these Monte Carlo simulations.

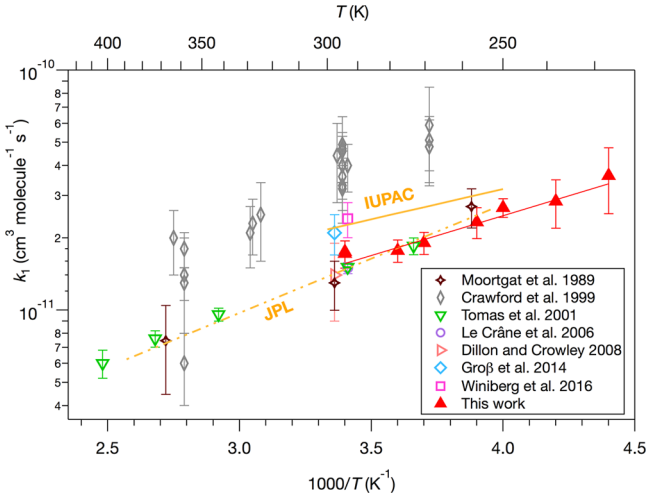

Figure 13. Temperature dependence of overall rate constant, k_1, determined in this work (red triangles) compared to previous works and to JPL (dash-dotted line) and IUPAC (solid line) recommendations.

4. DISCUSSION

4.1. Overall Rate Constant of the HO_2 + $CH_3C(O)O_2$ Reaction. The value of k_1 measured at room temperature and P = 100 Torr appear to be in good agreement with a majority of the previous values measured over a wide range of pressures (Table 6). While not explicitly stated, the JPL recommendation assumes that k_1 is pressure-independent. Our values are at the lower end of the range presented by Groß et al.[17] and Winiberg et al.,[18] but are still within experimental error. Our results are also significantly lower than the values reported by Crawford et al.[20] The higher rate constants reported by Crawford et al.[20] may be due to the high initial radical and precursor concentrations that were used. Under their experimental conditions, significant concentrations of adducts are expected, even at room temperature. Although additional HO_2 loss by reaction with CH_3CHO was taken into account, rate enhancement by CH_3OH was not, which would overestimate the HO_2 + $CH_3C(O)O_2$ rate constant.

Figure 13 compares the temperature dependence of k_1 with previous results. The observed temperature dependence agrees with the IUPAC values within 1σ, but the overall rate constant appears to be in better agreement with the JPL values due to a difference of almost a factor of 8 between the two recommended A-factors (Table 7). The agreement in the observed overall rate constant with the JPL values is rather fortuitous since the recommended values were based on the Tomas et al.[21] and Moortgat et al.[19] studies, which did not include radical recycling by the OH channel. Therefore, the previously reported rate constants were likely underestimated, which is consistent with what is observed in this work if we extrapolated to higher temperatures. At lower temperatures, the recommended values appear to be slightly larger than the values determined in this work, which may be due to insufficiently accounting for rate enhancement effects as mentioned before.

Figure 14 compares our room temperature values of the branching yields of (R1) to previous results that did not exclude OH recycling. All three product channels are consistent with previous measurements within 1σ. Our values for α_{1c} are also in good agreement with the more recent studies that used direct OH detection.[16−18] Slightly lower OH yields were reported by chamber studies.[9,15] Chamber-type studies require complex kinetics models to determine rate constants and branching yields from end-product analysis of stable products. Because they are more sensitive to wall-loss and secondary reactions that occur on longer time scales, systematic errors in the chemical model may

DOI: 10.1021/acs.jpca.9b00442
J. Phys. Chem. A 2019, 123, 3655−3671

Table 7. Comparison of Previous Temperature Dependence Studies and Current Results

ref	T (K)	A factor ($\times 10^{-12}$ cm^3 s^{-1})	E/R (K)	α_{1a}	α_{1b}	α_{1c}
Moortgat et al.[19]	253−368	0.43	−1040 ± 100	0.67 ± 0.07	0.33 ± 0.07	[a]
Horie and Moortgat[11]	263−333			$\alpha_{1a}/\alpha_{1b} = 330 \exp[(-1430 \pm 480/T)]$		[a]
Crawford et al.[20]	269−363	0.39	−1350 ± 250	0.88 ± 0.02	0.12 ± 0.04	[a]
Tomas et al.[21]	273−403	0.64	−925 ± 120	0.80 ± 0.02	0.20 ± 0.02	[a]
IUPAC[1]	250−230	3.14	−580 ± 400	$\alpha_{1a}/\alpha_{1b} = 340 \exp[(-1430 \pm 500/T)]$		
				$\alpha_{1c}/\alpha_{1b} = 2.34 \times 10^4 \exp[(-2600 \pm 3000/T)]$		
JPL,[29] Tyndall et al.[30]	253−403	0.43	−1040	0.80	0.20	[a]
this work	230−294	$1.38^{+1.17}_{-0.63}$	−730 ± 170	see Table 3 and Figure 11		

[a]Assumed $\alpha_3 = 0$.

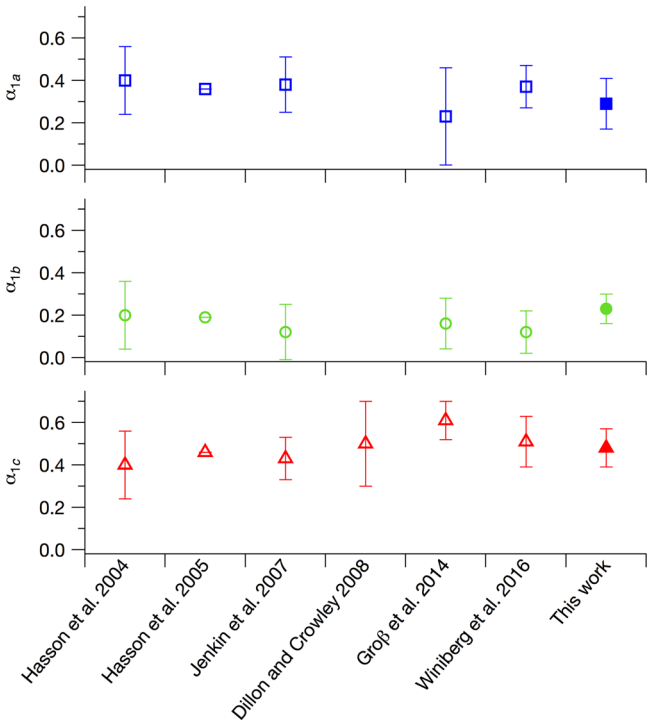

Figure 14. Comparison of room temperature values of α_{1a} (blue squares), α_{1b} (green circles), and α_{1c} (red triangles) measured in this work (2σ uncertainties) to previously reported values in the literature. Results from studies that assumed no OH recycling have been excluded.

explain the observed discrepancies with studies employing direct OH detection.

What we contribute to the efforts made to characterize the product distribution of this reaction is the temperature dependence. The trends that were observed (Figure 11) are consistent with the theoretical prediction by Hasson et al.,[13] who postulated that while the peracetic acid channel proceeds via hydrogen transfer, the OH and O_3 channels are interlinked by a common hydrotetroxide intermediate. The peracetic acid channel is relatively temperature-independent over this temperature range, consistent with the IUPAC recommendation and Hasson et al.'s theoretical values.[13] The overall trend of the OH and O_3 branching yields also appears to agree with IUPAC and with theory. It can be speculated that at higher temperatures, entropy favors the OH channel over the O_3 channel, which has a tighter transition state. The observed OH yield has a weaker temperature dependence compared to the IUPAC recommendations, leading to a larger OH yield at lower temperatures than was previously predicted.

5. CONCLUSIONS

The present work reports the first temperature dependence investigation of the OH product channel of the HO_2 + $CH_3C(O)O_2$ reaction using techniques that enabled direct detection of HO_2 and OH radicals combined with UV absorption measurements in real time. Also of importance is the extension to lower temperatures of the range of temperatures over which the overall rate constant has been previously measured, which has more relevance for atmospheric chemistry.

Analysis of data required using a complex kinetics model to disentangle the secondary chemistry, particularly (R8) and (R13). Estimated values of k_8, k_{13}, and α_{13a} were found to be within the uncertainty bounds of the recommended values from the current JPL data evaluation;[29] nonetheless, further reinvestigation of the kinetics and product yields of these reactions is clearly needed.

This work has shown that that significant rate enhancement of the HO_2 self-reaction was observed, which should be taken into account for accurate characterization of the HO_2 + $CH_3C(O)O_2$ reaction. Perhaps fortuitously, the rate constant of the title reaction appears to agree better with the JPL recommendation. Finally, our results suggest that especially at lower temperatures, higher OH regeneration may need to be included in atmospheric models.

■ ASSOCIATED CONTENT

Supporting Information

The Supporting Information is available free of charge on the ACS Publications website at DOI: 10.1021/acs.jpca.9b00442.

Detailed summary of experimental conditions at each temperature, time-dependent UV absorption signals shown with relative contributions from the main absorbers, Arrhenius plots from empirically determined values of k_8 and k_{13}, and fitted values of k_1 plotted as a function of $[HO_2]_0/[CH_3C(O)O_2]_0$ (PDF)

■ AUTHOR INFORMATION

Corresponding Authors

*E-mail: aileenh@caltech.edu.
*E-mail: mathieu.fradet@jpl.nasa.gov.
*E-mail: mo@caltech.edu.
*E-mail: stanley.p.sander@jpl.nasa.gov.

ORCID

Aileen O. Hui: 0000-0003-4217-2698
Mitchio Okumura: 0000-0001-6874-1137

Notes

The authors declare no competing financial interest.

DOI: 10.1021/acs.jpca.9b00442
J. Phys. Chem. A 2019, 123, 3655−3671

■ ACKNOWLEDGMENTS

This research was carried out by the Jet Propulsion Laboratory, California Institute of Technology, under contract with the National Aeronautics and Space Administration (NASA). The authors thank the Microdevices Lab (MDL) at the Jet Propulsion Laboratory (JPL), and in particular Mathieu Fradet and Siamak Forouhar, who were responsible for the fabrication of our mid-IR OH detection laser. Finally, A.O.H. thanks the National Science Foundation (NSF Grant No. CHE-1413712), the NASA Earth and Space Science Fellowship (NESSF), and NASA's Upper Atmospheric Research Program (UARP Grant No. NNX12AE01G), and Tropospheric Chemistry Program for financial support.

■ REFERENCES

(1) Atkinson, R.; Baulch, D. L.; Cox, R. A.; Hampson, R. F.; Kerr, J. A.; Troe, J. Evaluated Kinetic and Photochemical Data for Atmospheric Chemistry: Supplement IV. IUPAC Subcommittee on Gas Kinetic Data Evaluation for Atmospheric Chemistry. *J. Phys. Chem. Ref. Data* **1992**, *21*, 1125−1568.

(2) Tan, D.; Faloona, I.; Simpas, J. B.; Brune, W.; Shepson, P. B.; Couch, T. L.; Sumner, A. L.; Carroll, M. A.; Thornberry, T.; Apel, E.; Riemer, D.; Stockwell, W. HO x Budgets in a Deciduous Forest: Results from the PROPHET Summer 1998 Campaign. *J. Geophys. Res.-Atmos* **2001**, *106*, 24407−24427.

(3) Hofzumahaus, A.; Rohrer, F.; Lu, K.; Bohn, B.; Brauers, T.; Chang, C.-C.; Fuchs, H.; Holland, F.; Kita, K.; Kondo, Y.; et al. Amplified Trace Gas Removal in the Troposphere. *Science* **2009**, *324*, 1702−1704.

(4) Lu, K. D.; Rohrer, F.; Holland, F.; Fuchs, H.; Bohn, B.; Brauers, T.; Chang, C. C.; Häseler, R.; Hu, M.; Kita, K.; et al. Observation and Modelling of OH and HO_2 Concentrations in the Pearl River Delta 2006: A Missing OH Source in a VOC Rich Atmosphere. *Atmos. Chem. Phys.* **2012**, *12*, 1541−1569.

(5) Lou, S.; Holland, F.; Rohrer, F.; Lu, K.; Bohn, B.; Brauers, T.; Chang, C. C.; Fuchs, H.; Häseler, R.; Kita, K.; et al. Atmospheric OH Reactivities in the Pearl River Delta − China in Summer 2006: Measurement and Model Results. *Atmos. Chem. Phys.* **2010**, *10*, 11243−11260.

(6) Whalley, L. K.; Edwards, P. M.; Furneaux, K. L.; Goddard, A.; Ingham, T.; Evans, M. J.; Stone, D.; Hopkins, J. R.; Jones, C. E.; Karunaharan, A.; Lee, J. D.; Lewis, A. C.; Monks, P. S.; M?ller, S. J.; Heard, D. E. Quantifying the Magnitude of a Missing Hydroxyl Radical Source in a Tropical Rainforest. *Atmos. Chem. Phys.* **2011**, *11*, 7223−7233.

(7) Mao, J.; Ren, X.; Zhang, L.; Duin, D. M. V.; Cohen, R. C.; Park, J.-H.; Goldstein, A. H.; Paulot, F.; Beaver, M. R.; Crounse, J. D.; et al. Insights into Hydroxyl Measurements and Atmospheric Oxidation in a California Forest. *Atmos. Chem. Phys.* **2012**, *12*, 8009−8020.

(8) Fittschen, C.; Ajami, M. A.; Batut, S.; Ferracci, V.; Archer-Nicholls, S.; Archibald, A. T.; Schoemaecker, C. ROOOH: A Missing Piece of the Puzzle for OH Measurements in Low-NO Environments? *Atmos. Chem. Phys.* **2019**, *19*, 349−362.

(9) Hasson, A. S.; Tyndall, G. S.; Orlando, J. J. A Product Yield Study of the Reaction of HO_2 Radicals with Ethyl Peroxy ($C_2H_5O_2$), Acetyl Peroxy ($CH_3C(O)O_2$), and Acetonyl Peroxy ($CH_3C(O)CH_2O_2$) Radicals. *J. Phys. Chem. A* **2004**, *108*, 5979−5989.

(10) Niki, H.; Maker, P. D.; Savage, C. M.; Breitenbach, L. P. FTIR Study of the Kinetics and Mechanism for Chlorine-Atom-Initiated Reactions of Acetaldehyde. *J. Phys. Chem.* **1985**, *89*, 588−591.

(11) Horie, O.; Moortgat, G. K. Reactions of $CH_3C(O)O_2$ Radicals with CH_3O_2 and HO_2 between 263 and 333 K. A Product Study. *J. Chem. Soc., Faraday Trans.* **1992**, *88*, 3305−3312.

(12) Andersen, M.; Hurley, M.; Wallington, T.; Ball, J.; Martin, J.; Ellis, D.; Mabury, S. Atmospheric Chemistry of C_2F_5CHO: Mechanism of the $C_2F_5C(O)O_2$ + HO_2 Reaction. *Chem. Phys. Lett.* **2003**, *381*, 14−21.

(13) Hasson, A. S.; Kuwata, K. T.; Arroyo, M. C.; Petersen, E. B. Theoretical Studies of the Reaction of Hydroperoxy Radicals (HO_2) with Ethyl Peroxy ($CH_3CH_2O_2$), Acetyl Peroxy ($CH_3C(O)O_2$), and Acetonyl Peroxy ($CH_3C(O)CH_2O_2$) Radicals. *J. Photochem. Photobiol., A* **2005**, *176*, 218−230.

(14) Le Crâne, J.-P.; Rayez, M.-T.; Rayez, J.-C.; Villenave, E. A Reinvestigation of the Kinetics and the Mechanism of the $CH_3C(O)O_2$ + HO_2 Reaction Using Both Experimental and Theoretical Approaches. *Phys. Chem. Chem. Phys.* **2006**, *8*, 2163−2171.

(15) Jenkin, M. E.; Hurley, M. D.; Wallington, T. J. Investigation of the Radical Product Channel of the $CH_3C(O)O_2$ + HO_2 Reaction in the Gas Phase. *Phys. Chem. Chem. Phys.* **2007**, *9*, 3149−3162.

(16) Dillon, T. J.; Crowley, J. N. Direct Detection of OH Formation in the Reactions of HO_2 with $CH_3C(O)O_2$ and Other Substituted Peroxy Radicals. *Atmos. Chem. Phys.* **2008**, *8*, 4877−4889.

(17) Groß, C. B. M.; Dillon, T. J.; Schuster, G.; Lelieveld, J.; Crowley, J. N. Direct Kinetic Study of OH and O_3 Formation in the Reaction of $CH_3C(O)O_2$ with HO_2. *J. Phys. Chem. A* **2014**, *118*, 974−985.

(18) Winiberg, F. A. F.; Dillon, T. J.; Orr, S. C.; Groß, C. B. M.; Bejan, I.; Brumby, C. A.; Evans, M. J.; Smith, S. C.; Heard, D. E.; Seakins, P. W. Direct Measurements of OH and Other Product Yields from the HO_2 + $CH_3C(O)O_2$ Reaction. *Atmos. Chem. Phys.* **2016**, *16*, 4023−4042.

(19) Moortgat, G.; Veyret, B.; Lesclaux, R. Absorption Spectrum and Kinetics of Reactions of the Acetylperoxy Radical. *J. Phys. Chem.* **1989**, *93*, 2362−2368.

(20) Crawford, M. A.; Wallington, T. J.; Szente, J. J.; Maricq, M. M.; Francisco, J. S. Kinetics and Mechanism of the Acetylperoxy + HO_2 Reaction. *J. Phys. Chem. A* **1999**, *103*, 365−378.

(21) Tomas, A.; Villenave, E.; Lesclaux, R. Reactions of the HO_2 Radical with CH_3CHO and $CH_3C(O)O_2$ in the Gas Phase. *J. Phys. Chem. A* **2001**, *105*, 3505−3514.

(22) Christensen, L. E.; Okumura, M.; Hansen, J. C.; Sander, S. P.; Francisco, J. S. Experimental and Ab Initio Study of the HO_2·CH_3OH Complex: Thermodynamics and Kinetics of Formation. *J. Phys. Chem. A* **2006**, *110*, 6948−6959.

(23) Andersson, B. Y.; Cox, R. A.; Jenkin, M. E. The Effect of Methanol on the Self Reaction of HO_2 Radicals. *Int. J. Chem. Kinet.* **1988**, *20*, 283−295.

(24) Bloss, W. J.; Rowley, D. M.; Cox, R. A.; Jones, R. L. Rate Coefficient for the BrO + HO_2 Reaction at 298 K. *Phys. Chem. Chem. Phys.* **2002**, *4*, 3639−3647.

(25) Christensen, L. E.; Okumura, M.; Sander, S. P.; Friedl, R. R.; Miller, C. E.; Sloan, J. J. Measurements of the Rate Constant of HO_2 + NO_2 + N_2 →HON_2O_2 + N_2Using Near-Infrared Wavelength-Modulation Spectroscopy and UV-Visible Absorption Spectroscopy. *J. Phys. Chem. A* **2004**, *108*, 80−91.

(26) Noell, A. C.; Alconcel, L. S.; Robichaud, D. J.; Okumura, M.; Sander, S. P. Near-Infrared Kinetic Spectroscopy of the HO_2 and $C_2H_5O_2$ Self-Reactions and Cross Reactions. *J. Phys. Chem. A* **2010**, *114*, 6983−6995.

(27) Grieman, F. J.; Noell, A. C.; Davis-Van Atta, C.; Okumura, M.; Sander, S. P. Determination of Equilibrium Constants for the Reaction Between Acetone and HO_2 Using Infrared Kinetic Spectroscopy. *J. Phys. Chem. A* **2011**, *115*, 10527−10538.

(28) Keller-Rudek, H.; Moortgat, G. K.; Sander, R.; Sörensen, R. The MPI-Mainz UV/VIS Spectral Atlas of Gaseous Molecules of Atmospheric Interest. *Earth System Science Data* **2013**, *5*, 365−373.

(29) Burkholder, J. B.; Sander, S. P.; Abbatt, J.; Barker, J. R.; Huie, R.; Kolb, C. E.; Kurylo, M.; Orkin, V.; Wilmouth, D.; Wine, P. H. Chemical Kinetics and Photochemical Data for Use in Atmospheric Studies. *Evaluation No. 15*; JPL, 2015.

(30) Tyndall, G. S.; Cox, R. A.; Granier, C.; Lesclaux, R.; Moortgat, G. K.; Pilling, M. J.; Ravishankara, A. R.; Wallington, T. J. Atmospheric Chemistry of Small Organic Peroxy Radicals. *J. Geophys. Res.-Atmos* **2001**, *106*, 12157−12182.

(31) Fradet, M.; Hosoda, T.; Frez, C.; Shterengas, L.; Sander, S.; Forouhar, S.; Belenky, G. First Demonstration of Single-Mode Distributed Feedback Type-I GaSb Cascade Diode Laser Emitting

DOI: 10.1021/acs.jpca.9b00442
J. Phys. Chem. A 2019, 123, 3655−3671

near 2.9 μm. *Novel In-Plane Semiconductor Lasers XV*; SPIE, 2016; p 97670U.
(32) *FACSIMILE*; MCPA Software Ltd, 2003.
(33) *HITRAN on the Web*; http://hitran.org/, 2016.
(34) Hui, A. O. Atmospheric Peroxy Radical Chemistry Studied by Infrared Kinetic Spectroscopy. *Ph.D.*, California Institute of Technology, Pasadena, CA, 2019.
(35) Hui, A. O.; Okumura, M.; Sander, S. P. Temperature Dependence of the Reaction of Chlorine Atoms with CH_3OH and CH_3CHO. Manuscript Submitted for Publication.
(36) Roehl, C. M.; Bauer, D.; Moortgat, G. K. Absorption Spectrum and Kinetics of the Acetylperoxy Radical. *J. Phys. Chem.* **1996**, *100*, 4038−4047.
(37) Maricq, M. M.; Szente, J. J. The $CH_3C(O)O_2$ Radical. Its UV Spectrum, Self-Reaction Kinetics, and Reaction with CH_3O_2. *J. Phys. Chem.* **1996**, *100*, 4507−4513.
(38) Villenave, E.; Lesclaux, R. Kinetics of the Cross Reactions of CH_3O_2 and $C_2H_5O_2$ Radicals with Selected Peroxy Radicals. *J. Phys. Chem.* **1996**, *100*, 14372−14382.
(39) Assaf, E.; Song, B.; Tomas, A.; Schoemaecker, C.; Fittschen, C. Rate Constant of the Reaction between CH_3O_2 Radicals and OH Radicals Revisited. *J. Phys. Chem. A* **2016**, *120*, 8923−8932.
(40) Clegg, S. M.; Abbatt, J. P. D. Oxidation of SO_2 by H_2O_2 on Ice Surfaces at 228 K: A Sink for SO_2 in Ice Clouds. *Atmos. Chem. Phys.* **2001**, *1*, 73−78.
(41) Christensen, L. E.; Okumura, M.; Sander, S. P.; Salawitch, R. J.; Toon, G. C.; Sen, B.; Blavier, J.-F.; Jucks, K. W. Kinetics of $HO_2 + HO_2 \rightarrow H_2O_2 + O_2$: Implications for Stratospheric H_2O_2. *Geophys. Res. Lett.* **2002**, *29*, 13-1−13-4.
(42) da Silva, G.; Bozzelli, J. W. Role of the α-Hydroxyethylperoxy Radical in the Reactions of Acetaldehyde and Vinyl Alcohol with HO_2. *Chem. Phys. Lett.* **2009**, *483*, 25−29.
(43) Atkinson, R.; Baulch, D. L.; Cox, R. A.; Crowley, J. N.; Hampson, R. F.; Hynes, R. G.; Jenkin, M. E.; Rossi, M. J.; Troe, J. IUPAC Subcommittee, Evaluated Kinetic and Photochemical Data for Atmospheric Chemistry: Volume II − Gas Phase Reactions of Organic Species. *Atmos. Chem. Phys.* **2006**, *6*, 3625−4055.
(44) Noell, A. C. Laboratory Studies of the Self and Cross Reactions of Atmospheric Peroxy Radicals. *Ph.D.*, California Institute of Technology, Pasadena, CA, 2009.

■ NOTE ADDED AFTER ASAP PUBLICATION

This paper was published ASAP on April 17, 2019, with an error in the Abstract. The corrected version was reposted on April 22, 2019.

DOI: 10.1021/acs.jpca.9b00442
J. Phys. Chem. A 2019, 123, 3655−3671